Chemical Engineering & Processing: Process Intensification 176 (2022) 108934

Contents lists available at ScienceDirect

Chemical Engineering and Processing - Process Intensification

journal homepage: www.elsevier.com/locate/cep

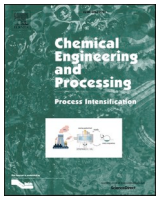

Supercritical fluid reactive deposition: A process intensification technique for synthesis of nanostructured materials

H. Yousefzadeh [a], I.S. Akgün [a], S.B. Barim [a], T.B. Sari [a], G. Eris [b], E. Uzunlar [b,c], S.E. Bozbag [a], C. Erkey [a,d,*]

[a] Department of Chemical and Biological Engineering, Koç University, Sarıyer, Istanbul, Turkey
[b] Iongenics Electrochemical Technologies, Urla, Izmir, Turkey
[c] Department of Chemical Engineering, İzmir Institute of Technology, Urla, İzmir, Turkey
[d] Koç University Tüpraş Energy Center (KUTEM), Koç University, Sarıyer, Istanbul, Turkey

A B S T R A C T

Supercritical fluid reactive deposition (SFRD) is a promising process intensification technique for synthesis of a wide variety of nanostructured materials. The enhanced mass transfer characteristics of supercritical fluids (SCFs) coupled with high solubilities of reducing gases in SCFs provide many advantages related to equipment size and time minimization over conventional techniques. Among SCFs, the emphasis has been placed on supercritical CO_2 ($scCO_2$) which is non-toxic, cheap and leaves no residue on the treated medium. Moreover, in SFRD, multiple processes such as dissolution, adsorption, reaction, and purification are combined in a single piece of equipment which is an excellent example of process integration for process intensification. In this review, the fundamental thermodynamic and kinetic aspects of the technology are described in detail. The studies in the literature on synthesis of a wide variety of nanostructured materials including supported nanoparticles, films, and ion-exchanged zeolites by SFRD are reviewed and summarized. The applications of these materials as catalysts and sensors are described. The review hopes to lead to further studies on further development of this technology for a wide variety of applications.

1. Introduction

A supercritcal fluid (SCF) is a fluid simultaneously heated and compressed above its critical temperature and pressure (T_c, and P_c respectively). Fig. 1 shows the P-T phase diagram of a pure substance [1]. Critical point (CP) of a substance is the point at which the vapor-liquid equilibrium line terminates. In practice, the term is used to denote fluids in the approximate reduced temperature and pressure range $T_r = 0.95–1.10$; $P_r = 1.01–1.5$ ($T_r = T/T_c$, $P_r = P/P_c$) extending slightly into the subcritical region. In the SCF region, only a homogenous phase exists due to absence of phase boundaries [2]. Supercritical state can be easily reached for a large number of substances such as CHF_3, CO_2 and C_2H_6 at temperatures below 37°C making them attractive for the processing of heat-sensitive organic substances. Among the SCFs, supercritical CO_2 ($scCO_2$) is particularly attractive due to its low T_c (31°C) and P_c (7.38 MPa) and also because it is abundant, inexpensive, nonflammable, nontoxic and environmentally benign [3].

The thermophysical properties of a SCF are intermediate between those of a gas and a liquid and can be adjusted by slight changes in temperature and/or pressure. These properties are summarized in Table 1 [4]. SCFs have liquid-like densities, gas-like viscosities and kinematic viscosities, much higher diffusivities than liquids and zero surface tension. Density of a SCF can be varied easily by slight changes in temperature and pressure. The liquid-like density of SCFs makes them appropriate as solvents for a wide range of solutes. Since the solute solubility varies generally as a power law with respect to density, a modest change in either pressure or temperature, in the vicinity of the critical point, can alter this solvating power as well as its selectivity as a solvent over a wide range of compounds [5]. Fig. 2 shows the density behavior of $scCO_2$ with temperature and pressure. In the supercritical region at pressures near the critical point, increasing temperature leads to a dramatic decrease of density, meanwhile a slow decrease of density by increasing the temperature is seen at higher pressures [1,6]. Viscosity of a SCF also changes with temperature and pressure. Lower viscosities of SCFs provides higher fluidity and molecular mobility compared to liquids. The higher diffusivities of solutes in SCFs may results in enhanced mass transfer rates compared to organic solvents. Thanks to this property, SCFs can enhance the chemical reactions which are controlled by mass transfer. The zero surface tension of SCF not only permits better penetration and wetting of pores than liquid solvents do, but also avoids the pore collapse which can occur when certain nanostructured materials such as organic and silica aerogels (SAs) are

* Corresponding Author.
E-mail address: cerkey@ku.edu.tr (C. Erkey).

https://doi.org/10.1016/j.cep.2022.108934
Received 31 December 2021; Received in revised form 30 March 2022; Accepted 6 April 2022
Available online 8 April 2022

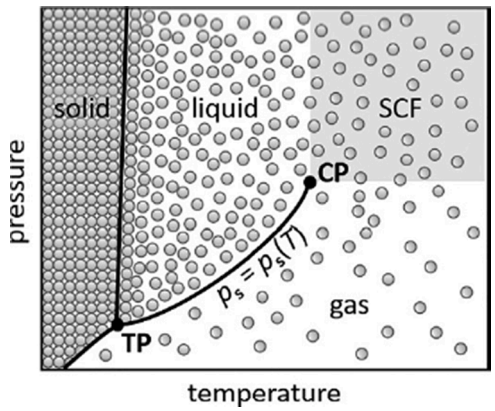

Fig. 1. Schematic P-T diagram of a pure substance (except water). Reprinted from [1], ©2021, with permission from Elsevier.

Table 1
Order of magnitude for typical thermophysical properties of gases, SCFs, and liquids [4].

Property	Unit	Gas	SCF	Liquid
Density (ρ)	kg m^{-3}	1	$5 \times 10^{+2}$	10^{+3}
Viscosity (η)	μPa s	10	10^{+1} to 10^{+2}	10^{+3}
Kinematic viscosity (ν)	m^2 s^{-1}	10	0.02 to 0.2	1
Diffusion coefficient (D_{12})	m^2 s^{-1}	10^{-5}	10^{-7} to 10^{-8}	10^{-9} to 10^{-10}

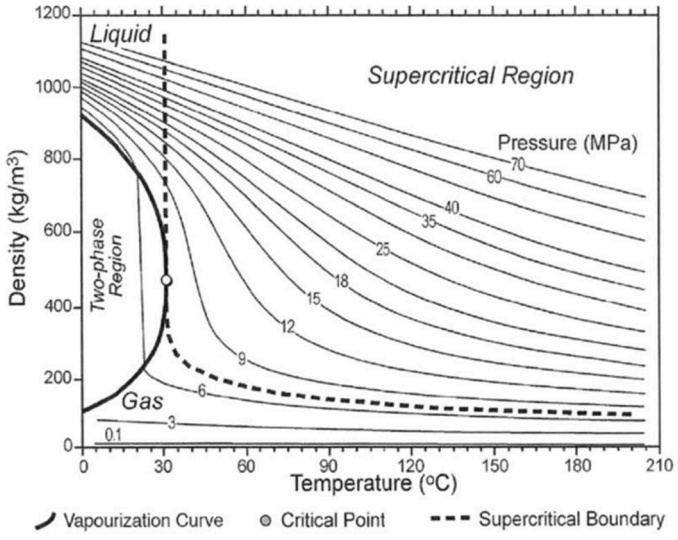

Fig. 2. CO_2 density behavior with temperature and pressure. Reprinted from [6],©2018, with permission form

contacted with liquid solvents [7]. $scCO_2$ also displays high permeation rate in virtually all polymers and the exposure to $scCO_2$ results in various extents of swelling and enhanced chain mobility of the polymers, which makes it possible to impregnate a wide variety of chemicals into various polymers [8]. Moreover, the degree of polymer swelling, diffusion rates within the substrate, and the partitioning of solutes between the SCF and the swollen polymer can be controlled by density mediated adjustments of solvent strength via changes in temperature and pressure [9]. $scCO_2$ is also miscible with gases including hydrogen, oxygen, and carbon monoxide at temperatures above its T_c. Therefore, significantly higher concentrations of such gases can be obtained in $scCO_2$ compared to organic solvents in which gases are sparingly soluble. Therefore, higher reaction rates can be obtained if the order of the reaction with respect to the gaseous substrate is positive [10]. $scCO_2$ is the most widely used SCF as solvent for synthesis of nanostructured materials due to its favorable physical and chemical properties. It is in gaseous state at ambient pressure which is one of the significant process advantages of $scCO_2$ to synthesize a completely solvent-free product without the need to use any thermal or mechanical post-treatments which are necessary in conventional methods [1,4].

Currently, large-scale chemical manufacturing is facing a serious solvent problem in connection with environmental concerns. Regulations concerning the use of hazardous organic solvents such as chlorinated hydrocarbons are becoming increasingly stringent and are thus spurring the development of environmentally friendly and economical processing media [11]. $scCO_2$ has excellent potential as an environmentally friendly and cheap medium. Increasing number of applications involving $scCO_2$ have been demonstrated in a variety of fields including polymerizations [12], pharmaceutical applications [13], textile processing [14] and dyeing [15], coatings [16], specialized materials fabrications, cleaning, chromatography [17], microelectronics processing [18], heterogeneous catalysis [19] and regeneration of adsorbents [20] and other solid matrices. Although specialized pressure vessels, high pressure pumps, and other equipment are necessary for processing, a remarkable number of successful commercial-scale processes such as natural products/food extractions, wood impregnation and aerogel production are being practiced on a commercial scale.

Supported metals, metal oxides and sulfides are frequently used in catalysis, electronics, and optics [21]. Such supported materials can exist in different morphologies such as atomically dispersed metals, nanoparticles (NPs), nanorods and thin films. Nanostructured materials are highly interesting scientifically and hold potential for a wide range of technological applications due to their higher surface-to-volume ratios. In NPs with very small particle size (PS), a significant fraction of the nanostructure is composed of interfaces/grain boundaries and hence a large fraction of the atoms resides in grain boundaries. In this size range, phenomena associated with atomic and molecular interactions strongly influence the macroscopic properties of materials and give rise to the unique electronic, optical, electro-optical, magnetic, and catalytic properties which are often superior to the properties of their conventional coarse-grained polycrystalline counterparts.

There are several ways to synthesize supported NPs, including impregnation, deposition–precipitation, co-precipitation, sonochemical reduction, chemical vapor impregnation, sol–gel and microemulsion using organic stabilizing agents [22]. The control over either particle dimensions, including the PS and particle size distribution (PSD), or metal concentration in the composites remains the major problems for these methods. For example, the traditional impregnation, deposition–precipitation and co-precipitation methods using liquid solutions as the processing medium could cause not only agglomeration of particles but also the collapse of the fragile supports such as SA or other organic aerogels due to the high surface tension of the liquid solutions. The conventional sol–gel route could be used to incorporate metal NPs into the structure of various types of porous materials. However, the metal complexes in solution interfere with the polymerization chemistry resulting in materials with undesirable properties [21,23]. Furthermore, sol–gel technology cannot be applied to polymeric substrates easily. The water-in-oil microemulsions which can be created using surfactants is another medium used for the synthesis of supported metallic NPs. However, surfactants could interfere with the direct attachment of the particle to support by affecting the metal–support interactions and the removal of the surfactant could result in agglomeration of the particles due to high temperatures [24]. Chemical vapor deposition (CVD) is another promising route to prepare supported metal NPs. In practice, however, it is often limited by the vapor pressure of the metal complex, the processing temperature requirements and mass-transfer-limited kinetics [22].

Deposition using supercritical fluids is a technology that has been attracting increasing attention to prepare metallic films and supported metallic nanoparticles. For synthesis of films, metallic complexes and a

reducing agent such as hydrogen react on surface to form metallic films. This film formation reactions occur while the fluid phase is in the supercritical state. It is therefore appropriate to call this technique supercritical fluid reactive deposition (SFRD). For the synthesis of supported nanoparticles, the first step is the adsorption of metal complexes on the surface of a porous support material. Adsorption occurs while the fluid phase is in the supercritical state. After adsorption, adsorbed metal complexes are converted to metallic nanoparticles using a variety of methods. These methods can be divided into two major categories:

1. The system is depressurized, and the conversion reactions are carried out in the presence of an inert gas such as nitrogen or in the presence of a reducing gas such as hydrogen at atmospheric pressure and at elevated temperatures or sometimes even at elevated pressures using hydrogen. These conversion reactions are not carried out in a SCF environment. Therefore, it is really not appropriate to term this kind of deposition SFRD.

2. The conversion reactions are also carried out in the presence of a SCF phase in one pot synthesis. In this case, the fluid phase is heated, or a reducing agent is injected to the high-pressure solution. Therefore, the conversion reactions occur in the presence of a SCF, and it is appropriate to term this kind of deposition SFRD.

A significant number of the studies in the literature on deposition using SCFs have been carried out using the first method [4,25,26]. The second method, SFRD, has many advantages. Process intensification generally involves process miniaturization and process integration. In the former, reduction in equipment size can be achieved through higher intensities for mixing and enhanced heat and mass transfer. In the latter, multiple process tasks can be combined in a single piece of equipment. SFRD involves both of these due to enhanced mass transfer mass transfer characteristics of SCFs and combining multiple tasks of solubilization, adsorption, nanoparticle formation and purification in the same vessel. Moreover, the high concentration of reducing gases in SCFs leads to very high rates of reactions associated with conversion of metal complexes to their metallic forms resulting in miniaturization of deposition vessels. This should minimize plant size of equipment capable to produce specific sized, high quality supported nanoparticles combined with an increase in energy efficiency, safety, and cost reduction. This review covers the studies in the literature on SFRD defined as above.

2. Supported nanoparticles synthesis using SFRD

Synthesis of supported nanoparticles using SFRD involves dissolution of metal complex in the supercritical fluid, adsorption of the metal complex from the supercritical fluid mixture on the surface of the porous support, conversion of adsorbed metal complex to metallic nanoparticle in presence of the supercritical fluid, and depressurization and purification. Synthesis of supported NPs are generally conducted in hot-wall reactors which are essentially isothermal furnaces. Therefore, uniform temperature distribution in the hot-wall reactors is obtained. Since both reactor and support are heated which lead to nucleation both on the surface of substrate and all over the vessel, selective deposition cannot be obtained in hot-wall reactors [27]. They are also widely used for CVD processes [28]. Fig. 3 shows the hot-wall reactor in batch mode. First, metal complex and support are placed in the reactor. A pump is generally used for the transfer of CO_2 from tank to the reactor which is pressurized via opening the inlet valve. A pressure transducer and a thermocouple are employed on the reactor to monitor the temperature and the pressure. The temperature of the vessel and the support is controlled by circulating a heating medium such as water or oil through the internal heating channel of the vessel. A magnetic stirrer is used to mix the contents of the reactor. After a certain time of dissolution and adsorption of the metal complex, it is reduced to the metallic form by either injecting a reducing agent such as H_2 or by thermal reduction which requires increasing the temperature of the vessel. Subsequently, the vessel is slowly depressurized and the materials in discharged from the vessel. The state of the art in all the steps of a SFRD process are described in more detail in the following sections.

2.1. Solubility of metal complexes in supercritical fluids

The solubility of solute in SCFs is affected by both vapor pressure of the solute and the density of SCF. The vapor pressure of a solute always increases with temperature while the density of the fluid decreases with increasing temperature [30]. Therefore, the effect of temperature on the solubility of the solute is more complicated. Increasing temperature of SCF while the pressure is between the lower and upper cross-over pressures (P_L, and P_U respectively) leads to a rapid decrease on the density [22]. The dominant effect of density in this region leads to decrease in solubility with increasing temperature. Solubility of a solute increases with increasing temperature above P_U and below P_L, since the effect of vapor pressure of the solute dominates [22,30].

Non-polar compounds have usually high solubilities in $scCO_2$ [31]. Solubility data of the metal complexes with different ligand types including dithiocarbonates, macrocycles and hydroxamic acids in $scCO_2$ are available in the literature [25]. Complexes with ligands such as, dithiocarbamate, phosphine and amine can also be solubilized in $scCO_2$ [3,32-34]. Another system whose solubility is extensively investigated in $scCO_2$ is β-diketonate metal complexes including metal acetylacetonate (acac), 2,2,6,6-tetramethyl-3,5- heptanedionate (thd), 2,2,6,6-tetramethyl-3,5-heptanedionate (thmd), hexafluoro acetylacetonate (hfac) [23,31]. Solubility data of various β-diketonate, cyclopentadienyl

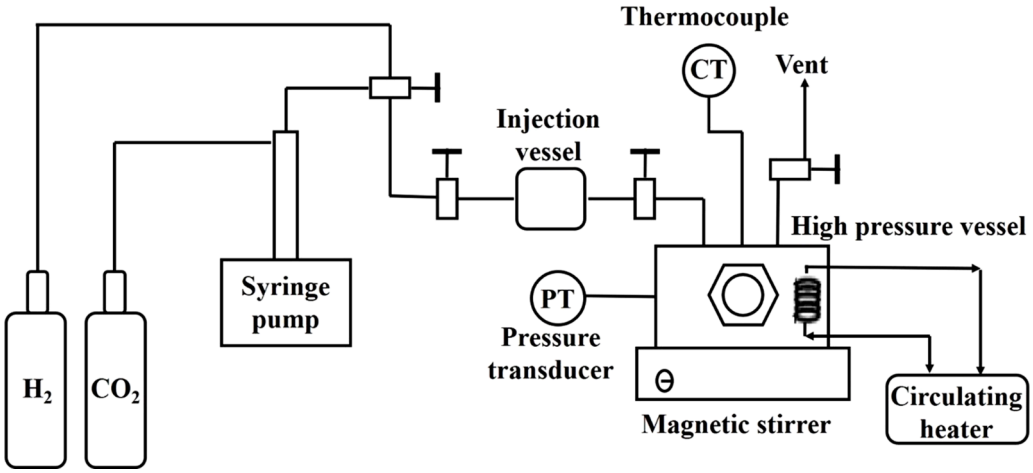

Fig. 3. Hot-wall reactor design in batch mode. Reperinted from [29],©2021, with permission from Elsevier.

(cp) and cyclooctadiene (cod) complexes with metals including silver, copper, nickel, palladium, rhodium, ruthenium, cobalt, chromium, iron, manganese, osmium, vanadium, platinum, potassium, rubidium, titanium, zinc and zirconium were measured by Aschenbrenner *et al.* [31] at a temperature of 60°C and pressures up to 30 MPa. It was found that solubility increases with increasing oxidation state of the metal atom for complexes with the same ligand. Moreover, a high atomic mass of the center atom causes a low solubility in $scCO_2$. Carbonyl ligands also lead to an increase in the solubility of a metal complex due to its specific intermolecular interactions with CO_2 [35].

In general, acac complexes have lower solubility than thd, cp and cod complexes. Substitution of methyl group in the acac ligand by tert-butyl groups improve solubility due to a better shielding of center atom that thd provides [31]. Moreover, addition of alkyl groups reduces cohesional energy density compared to acac leading to higher solubilities. For instance, Haruki *et al.* [36] measured the solubility of $Co(thd)_3$, $Co(acac)_3$, $Cr(thd)_3$, $Cr(acac)_3$ in $scCO_2$ at temperatures ranging from 40°C to 70°C and at pressures ranging from 10 to 19 MPa. They found that the solubilities of $Co(thd)_3$ in $scCO_2$ (2.8×10^{-3} mole fraction at 343 K, 190 bar) was 50 times higher than the solubility of $Co(acac)_3$ while 70 times higher solubility was achieved for $Cr(thd)_3$ (5.2×10^{-3} mole fraction at 70°C, 163 bar) than $Cr(acac)_3$. Fluorination of the alkyl groups also results in a significant enhancement in solubility [37,38]. For example, the solubility of $Cu(hfacac)_2$ and $Cr(hfacac)_3$ in $scCO_2$ are two orders of magnitude higher than their nonfluorinated analogues [23]. In another study, Özel *et al.* compared the solubilities of $Co(acac)_2$ and $Co(hfacac)_2$ in $scCO_2$ at 100°C and 40.5 MPa, and the results showed that the solubility of $Co(hfacac)_2$ (27×10^{-8} mol fraction) was about 7-fold higher than that of $Co(acac)_2$ (4×10^{-8} mol fraction) [39]. Higher volatility and decreased polarity of fluorinated compounds as compared to their non-fluorinated forms have been suggested as the possible reasons for their higher solubility [23,30]. Extensive compilation of the properties of metal complexes having high solubility in $scCO_2$ is reported in different books [22,40].

Besides the relatively non-polar metal complexes, inorganic polar precursors such as metal nitrates and chlorides may also be used for preparation of supported metal oxides using highly miscible alcohols with $scCO_2$ such as methanol or ethanol as cosolvents, or CO_2 expanded solutions. For instance, Eu_2O_3 [41], Al_2O_3 [42], Co_3O_4 [43], Fe_2O_3 [44], ZrO_2 [45], CeO_2 [46], Mn_3O_4 [47], Cr_2O_3 [48], and SnO_2 [49] on carbon nanotubes were obtained in $scCO_2$ + ethanol solutions in the temperature range of 100-150°C by using different metal nitrates. Factors affecting phase behavior such as temperature, pressure and concentration of metal complex of different hydrous inorganic metal salts ($Ni(NO_3)_2{\bullet}6H_2O$, $Fe(NO_3)_3{\bullet}9H_2O$, $Co(NO_3)_2{\bullet}6H_2O$ $Zn(NO_3)_2{\bullet}6H_2O$, $Cu(NO_3)_2{\bullet}3H_2O$, $Cr(NO_3)_3{\bullet}9H_2O$, $Nd(NO_3)_3{\bullet}6H_2O$, $SnCl_2{\bullet}4H_2O$, $MnCl_2{\bullet}4H_2O$) in $scCO_2$ + ethanol were investigated [50,51].

Prediction of the solubility of metal complexes in SCFs is possible using semi-empirical correlations or Equation of State based methods. For instance, Cross *et al.* utilized the Peng-Robinson equation of state to determine the solubilities of $Cu(acac)_2$ and $Cu(ddc)_2$ in $scCO_2$ [52]. Benedict-Webb-Rubin equation of state was used by Lagalante *et al.* to predict the solubility of $Cr(acac)_3$ in $scCO_2$ [37]. A good agreement was observed between experimental and predicted data at pressures above 30 MPa while the model underestimated the data by two orders of magnitude at pressures near 10 MPa. The correlation proposed by Chrastil is also promising model for prediction the solubilities of solutes in SCFs. For instance, Smart *et al.* [53] correlated the solubilities of 49 organometallic compounds in $scCO_2$ and Andersen *et al.* [54] correlated the solubilities of various β-diketonate metal complexes in $scCO_2$ in a wide range of temperatures and pressures using Chrastil model. Semi-empirical models such as Chrastil equation describes solubility as a function of density and temperature and can be utilized only for extrapolation of limited amount of data within a certain temperature and a pressure range [55]. One such good model alternative is the perturbed-chain statistical associating fluid theory (PC- SAFT) which has been widely used to model high pressure systems and could correlate the literature data over wide temperature and pressure ranges for various metal complexes. For instance, Ushiki *et al.* showed that PC-SAFT predictions accurately predicted the experimental solubilities of various acac-type metal complexes in $scCO_2$ with pressures ranging from 16 to 30 MPa and temperatures ranging from 278 to 303 K [55].

2.2. Adsorption from supercritical solutions

2.2.1. Thermodynamics of adsorption

Adsorption of metal complex(es) on high surface area support supports in the presence of $scCO_2$ is the second step of the SFRD process. The metal complex dissolved in $scCO_2$ is transferred to the surface by external mass transfer and pore diffusion followed by adsorption on surface sites of the support.

At equilibrium, the amount of adsorbed metal complex depends on the concentration of the metal complex in $scCO_2$-metal complex solution. This behavior is thermodynamically represented by an adsorption isotherm which is a function depicting the variation of surface uptake with respect to concentration in the $scCO_2$ phase. Adsortion thermodynamic analysis for a variety of metal complex-support system in the presence of $scCO_2$ are available and the articles on this matter can be found in [5,23,25,26,56-58]. Here, the general principles and fundamentals of the metal complex adsorption process in $scCO_2$ will be described with selected examples. Exemplary adsorption isotherms of Nickel(II) acetylacetonate ($Ni(acac)_2$) and bis(1,1,1,3,5,5,6,6,6-nonafluorohexane-2,4-diiminate)copper (CuDI6) on carbon aerogel (CA) in the presence of $scCO_2$ are given in Fig. 4a and b, respectively. Fig. 4a shows a Henry's type adsorption isotherm (Eq. 1) where the uptake (q_i, where i is the metal complex) is a linear function of the metal complex concentration (C_i) in $scCO_2$ which are correlated by Henry's adsorption constant, k. Fig. 4b show a Langmuir type adsorption isotherms (Eq. 2-3) where metal complex uptake plateaus at a certain concentration around 6 mol/m^3.

$$q_i = kC_i \tag{1}$$

$$\theta_i = \frac{Kp_i}{1 + Kp_i} \tag{2}$$

$$q_i = \frac{K_0 Q_0 C_i}{1 + K_0 C_i} \tag{3}$$

Eq.2 shows the general form of Langmuir adsorption isotherm equation where θ_i is the fractional coverage of species *i*, K is the adsorption equilibrium constant and p_i is the equilibrium partial pressure of species i. For adsorption processes in solution Eq.2 is usually written in the form of Eq. 3 where q_i is the uptake of species *i*, K_0 is the adsorption equilibrium constant, Q_0 is the uptake capacity and C_i is the equilibrium concentration of species *i*. The reason for observing two different types of isotherms lies on the fact that two metal complexes in question i.e. $Ni(acac)_2$ and CuDI6 have quite different solubility values in $scCO_2$. The last point of the isotherm in Fig. 4a is associated with the solubility of $Ni(acac)_2$ in $scCO_2$ which is low. On the other hand, CuDI6 has higher solubility and thus it can be used at higher equilibrium concentrations in $scCO_2$ which translates into higher uptakes. The plateau in the adsorption isotherm is associated with the saturation of the surface sites assuming monolayer coverage. The differences in the slopes of the initial points of the isotherms are associated with the surface favorability towards the metal complex. This is very well illustrated in Fig. 4b where the adsorption isotherms of CuDI6 on different supports are given. Here the most favorable isotherm is the one with the CuDI6-$scCO_2$-CA system since the same uptake is reached at lower equilibrium concentrations as compared to those with resorcinol formaldehyde aerogels (RFA) or silica aerogels (SA). This is most probably due to the differences in surface affinities. The understanding of this behavior is of high importance since the interactions of the support surface with metal

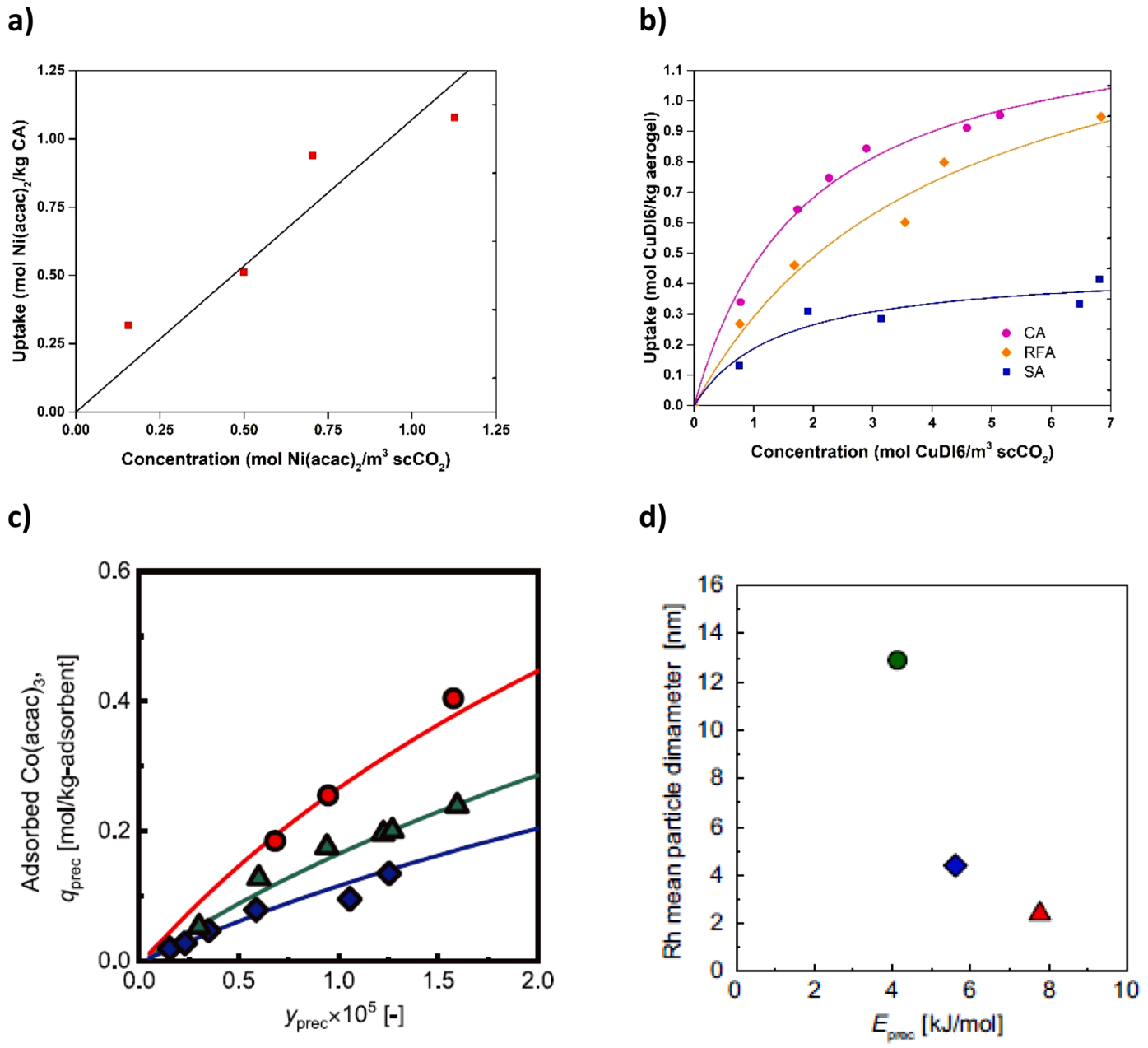

Fig. 4. (a) Adsorption isotherm of $Ni(acac)_2$-CA system in $scCO_2$ at 30 MPa and 60 °C, data adapted from [63], (b) Adsorption isotherms of CuDIA on CA, RFA and SA in $scCO_2$ at 10.6 MPa and 35 °C, data adapted from [64], (c) Pressure dependence of the adsorption equilibria of Co(acac)3 on MCM-41 in scCO2 with methanol co-solvent at 333 K (spheres: 12.5 MPa; triangles: 15.0 MPa; tilted squares: 20.0 MPa; solid lines were generated by the Dubinin-Astakhov correlation). Reprinted from [59], ©2018, with permission from Elsevier (d) Variation of the size of the supported rhodium oxide NPs prepared by SFRD with respect to adsorption energy. Reprinted from [60],©2017, with permission from Elsevier.

complex may determine the mechanism of which the metal complexes decompose and convert to metal. Ushiki *et al.* showed that the adsorption isotherms of $Co(acac)_3$ on MCM-41 (Fig. 4c) [59] and $Rh(acac)_3$ on different mesoporous silicas such as MCM-41, MSU-H and HMS [60] in the presence of $scCO_2$ and methanol co-solvent could be represented by Dubinin-Astakhov (DA) isotherm equation (Eq 4-6) which is a semi-empirical thermodynamic equation which relates the fugacities of the solute in solid and fluid phases to the uptake [61].

$$W_i = W_{0,i}\exp\left[-\left(\frac{\varepsilon_i}{E_i}\right)^n\right] \tag{4}$$

where ε_i is given by

$$\varepsilon_i = RT\ln\left[\frac{f_i^{sat}(T)}{f_i(T,P,y_i)}\right] \tag{5}$$

where f_i^{sat} and f_i are the fugacity of species i as saturated vapor and in the high pressure fluid phase, respectively. and

$$q_i = \frac{\rho_i^{ads} W_i}{M_i} \tag{6}$$

where ρ_i^{ads} is the density of the metal complex in the adsorbate state and M_i is the molecular weight of species *i*.

In Eq. 4, W_i and $W_{0,i}$ are the adsorbate volume and adsorbate volume at saturation per adsorbent mass. ε_i is the adsorption potential of the metal complex which is described in Eq. 5 and E_i is the interaction

energy between metal complex and support. Fugacity of metal complex in the SCF phase in Eq. 5 can be obtained using an equation of state (EOS) such as Peng-Robinson EOS if the binary interaction parameter between solvent and solute is known. Although thermodynamically based adsorption isotherm modeling is not a new concept [62], advantages of the DA isotherm equation is the simplicity and the fact that it readily contains the E_i term which gives a quantification of the metal complex-support interaction. Along this line, a correlation could be obtained between the interaction energy of a metal complex and the size of the metal NPs formed subsequently as illustrated in Fig. 4.d which shows a decreasing trend in nanoparticle size as the interaction energy between metal complex and support is increased. This observation could be manifesting due to a variety of reasons such as decreased metal complex reaction rates during its conversion to metal nanoparticle and/or decreased surface diffusion rate due to strong adsorption. This points out to the significance of the detailed analysis and understanding of the metal complex adsorption thermodynamics for the elucidation supported NP formation process. However, caution must be taken for creating such correlations, for instance, a variety of other parameters such as the metal wt. % (i.e. Rh wt. %, which was not the same for all the samples used in [60]) or the temperature at which the metal complex conversion occurs are affecting NP growth, thus the effect of adsorption energy on the formed PS is somewhat less clear. Another factor of concern is the fact that the DA isotherm requires the knowledge of density of the metal complex in the adsorbed phase which was assumed to be equal to the solid density of the metal complex which may not be reasonable assumption considering the uncertainties associated with excess uptakes. Moreover, the DA isotherm assumes liquefaction of metal complex within the pore volume, the validity of this assumption under SCF conditions needs testing. Nevertheless, this study is a good example on unifying the thermodynamic analysis of metal complex adsorption to the supported NP formation.

As previously mentioned, one of the most important properties of SCFs, is the fact that the thermo-physical properties such as the solvation power can easily be tuned via changes in pressure and temperature of the process. Unlike conventional solvents, these changes have important consequences on the behavior of the adsorption isotherm. It has been shown that the increase in pressure at a constant temperature (i.e. increase in $scCO_2$ density) during the adsorption step resulted in the decreased uptake at a certain equilibrium concentration of the metal complex [59] as illustrated in Fig. 4c. The effect of temperature on the uptake at a certain concentration is somehow more complex. The conventional wisdom dictates the increase of the desorption rate constant with increasing temperature for a single adsorbate desorption from a surface. However, although in many cases, the uptake of the metal complex decreased with increasing temperature (at a certain pressure) [57], due a combined effect of the cross-over phenomena associated with the solute dissolution in $scCO_2$ [65] and the excess adsorption of CO_2 on the support giving rise to a competition between CO_2 and metal complex, increase in temperature may result in higher uptakes [60,64]. Individual isotherm equation fits using Langmuir or other type of expressions usually results in a good representation of the experimental data. However, at this point, the literature still lacks a detailed thermodynamic analysis of the metal complex-$scCO_2$-support system based on the equity of the fundamental fugacity derivatives employed for other solute-$scCO_2$-support systems in the literature [66–68] which encompasses CO_2 adsorption as well. Another approach to enhance adsorption of metal complexes on supports in the presence of $scCO_2$ is the utilization of co-solvents such as alcohols [59,69] which enhances the dissolution of solutes otherwise less soluble in $scCO_2$. Thermodynamic analysis carried out by [59] for $Co(acac)_3$ adsorption on MCM-41 in the presence of $scCO_2$ and methanol as co-solvent showed that this approach results in lowered metal complex uptake as compared to the case without co-solvent due to the competitive adsorption between methanol and $Co(acac)_3$.

Thermodynamics of adsorption of multicomponent mixtures of metal complexes in the presence of $scCO_2$ is also complex. The only study to date on this matter was carried out by Bozbag *et al.* who investigated the thermodynamics of binary adsorption of CuDI6 and platinum(II) (1,5-Cyclooctadiene)dimethyl ($Pt(cod)(me)_2$) on CAs in the presence of $scCO_2$. For the binary adsorption equilibrium of the metal complexes, it was shown that the uptake of CuDI6 and $Pt(cod)(me)_2$ both decreased with increasing equilibrium concentrations of the other metal complex as compared to the uptake associated with single adsorption isotherms due to the competition on surface sites. This behavior was very well modeled using the Ideal Adsorbed Solution Theory (IAST) (which is analogous with Raoult's law). Both equilibrium concentrations and uptakes measured experimentally at 10.6 MPa and 35 °C were very well predicted using IAST in conjunction with the single adsorption isotherms of the individual metal complex without the requirement of any additional fitting parameter for binary adsorption. This showed that, for the case of investigation, the adsorption of a secondary metal complex did not affect the adsorption isotherm parameters of the other one, i.e. they did not interact with each other. To generalize this thesis, more studies are necessary at other pressure and temperature conditions and using other metal complex(es)-$scCO_2$-support systems.

2.2.2. *Kinetics of Adsorption*

Adsorption of metal complexes from the SCF phase to the solid support phase is characterized in four consecutive steps: (i) mass transfer of metal complex from bulk SCF phase to the surface of the adsorbent (ii) pore diffusion in adsorbent phase (iii) adsorption onto the surface of the adsorbent in the pores (iv) surface diffusion [70].

Transport properties, such as viscosity of SCF and binary diffusion coefficient of a solute in SCF affect the mass transfer rate of the solute in SCFs. Binary diffusion coefficient (D_{12}) can be tuned via changing pressure and temperature to improve transport properties of solubilized metal complexes in SCF. In general, D_{12} decreases with increasing pressure and increases with increasing temperature [4]. It was reported that D_{12} of both $Pd(acac)_2$ and $Co(acac)_3$ in $scCO_2$ decreases with pressure due to the strong increase of the density in the near critical region [71–73]. The fact that, at constant temperature and higher pressures, D_{12} decreases slightly with pressure is due to the lower increase of the fluid's density in that region. Furthermore, according to the Stokes-Einstein relation, D_{12} increases with temperature. Obviously, the binary diffusion coefficients of metal precursors in $scCO_2$ are significantly higher than in organic solvents such as ethanol. These higher D_{12} values lead to enhanced mass transfer rates in comparison to organic solvents causing higher fluxes inside the pores of a solid material. Thus, in the near or supercritical region liquid-like density and therewith solubility is combined with gas-like mass transfer rate.

Zhang *et al.* [74], Cangül *et al.* [75] and Bozbag *et al.* [76] developed a kinetic model of adsorption for ($Ru(cod)(tmhd)_2$) on CAs and $Pt(cod)(me)_2$ onto RFA, respectively. External mass transfer step was assumed negligible due to stirring employed. Local equilibrium for adsorption was assumed implying that the adsorbed phase concentration is linked to the concentration in the pore via adsorption isotherm. Hence, kinetics of the overall process is controlled by mass transfer occurring via diffusion of metal complex in the pores of the adsorbent. Then, the appropriate material balances were solved for the variation of pore phase metal complex concentration with time and distance. Effects of Modified Langmuir isotherm parameters were analyzed to evaluate the effect of adsorption capacity which makes the most significant influence on the kinetics, whereas the effect of adsorption equilibrium constant, although present, was small. Ushiki *et al.* [77] adapted the kinetic model of Zhang *et al.* for modeling the adsorption kinetics in their dynamic measurements. The main difference between the two studies was the calculation of the effective diffusivity of the metal complex inside the pores. Ushiki *et al.* modeled the effective diffusivity using tortuosity as the fitting parameter, and the adsorbent porosity was obtained from pore volume [78,79] and density of particles; binary diffusion coefficient of the metal complex and $scCO_2$ was obtained from the literature

[80]. Zhang *et al.* used the restriction factor, which is a function of solute and pore diameter in addition to porosity, tortuosity, and diffusion coefficient. Zhang *et al.*[74] was able to investigate the effect of solute and pore diameter on diffusion kinetics. When the pore size was decreased from 22 nm to 5 nm, the time required for equilibration increased from 1800 seconds to 3750 seconds according to the model, whereas almost no change was observed after increasing the pore size from 22 nm to 100 nm. Ushiki *et al.* reported that for a 40 ^{o}C increase in temperature, effective diffusivity of $Rh(acac)_3$ in $scCO_2$ increased to 4.5, 2.5, 2 fold for MSU-H, MCM41, HMS respectively.

Aschenbrenner [81] *et al.* studied the adsorption kinetics on two support geometries: monolith and silica gel particles. The rate of uptake of $Pt(cod)(me)_2$ onto monolith was much faster: equilibrium was reached after one hour, whereas in silica gel, it was more than three hours. It was observed that the monolith had a lower external mass transfer resistance as compared to the silica gel. Authors suggested that it was due to the larger specific external surface of the monolith (0.00602 m^2g^{-1}) compared to silica gel (0.00107 m^2/g). Ushiki *et al.* [82] also employed dynamic technique for kinetic measurement of adsorption of $Rh(acac)_3$ onto mesoporous silica adsorbents in a fixed bed column. Adsorption kinetics was modeled including external mass transfer from bulk phase to the adsorbent surface. External mass transfer coefficient was calculated using self-diffusion coefficients of $scCO_2$ obtained from Liu *et al.*'s study [83]. Axial dispersion coefficient for the bulk flow was obtained from Péclet number and Schmidt number correlation, again using self-diffusion coefficients of $scCO_2$. The variation of the bulk phase concentration with time at different points through the column were obtained by this model.

Kinetics of adsorption of binary metals (Pt-Cu) from $scCO_2$ on CA using $Pt(cod)(me)_2$ and CuDI6 was first reported by Bozbag *et al.*[84]. The authors suggest that detailed modeling studies are required for binary systems.

Sastre *et al.* [85] used pseudo-first-order and pseudo-second-order kinetic models for adsorption of nickolecene in MCM-48 and ruthenocene in MCM-48 and activated carbon. The pseudo-first-order model was found to represent the experimental data better for all three cases. They have used Weber-Morris plots [86] to separate external mass transfer, internal diffusion, and adsorption phenomena.

Although the models developed by Zhang *et al.* and Ushiki *et al.* agree well with the experimental data satisfactorily, improvement is still required to understand the kinetic processes better. The assumption of local equilibrium for adsorption might be omitted and kinetic mechanisms for adsorption and desorption of metal complexes in the presence of $scCO_2$ could be developed, and intrinsic rate constants for reactions could be obtained via a more detailed analysis. Bozbag *et al.*[76] pointed out to the surface diffusion effect during thermal treatment which was performed subsequent to adsorption step, adsorbed metal complexes or Pt NPs were found to be mobile on RFA. More investigations are necessary to elucidate the nature of surface diffusion in the presence of $scCO_2$. Furthermore, kinetic models developed in all the mentioned studies do not couple the adsorption kinetics with surface reactions. Further research and modeling efforts are required for better understanding the overall process.

2.3. Conversion of adsorbed metal complex to metal nanoparticles

The 3rd step of SFRD technique is conversion of the adsorbed meal complexes to their metallic form by a variety of reduction methods. The physical properties of the supported nanostructures including morphology, dispersion, PS and PSD can be tuned by the reduction method as well as the process parameters (reaction temperature and time) of the conversion step and one can end up with supported highly dispersed NPs, films, or rods. In the SFRD method, two different reduction approaches can be utilized as given below [5]:

I) chemical reduction in the SCF with a reducing agent, such as hydrogen or an alcohol
II) thermal reduction in the SCF

Chemical reduction is performed after a certain period of the metal complex adsorption on the support in SCF by adding a reducing agent such as H_2 or an alcohol to the SCF medium. This is followed by reduction reactions occurring between the metal complex molecules and the reducing molecules. The conversion reaction and the particle growth continue until H_2 or the metal complex in the fluid phase is consumed [25]. Thermal reduction of the adsorbed metal complexes molecules to metal form in supercritical medium is another approach to prepare supported metal NPs. In this method, instead of introducing a reducing agent, the fluid is heated up after a desired period of the metal complex adsorption, resulting in decomposition of the adsorbed metal complex molecules to elemental metal and formation of the metal NPs. As a result of adsorbed molecules decomposition, filled adsorption sites are vacated and re-filled with new metal complex molecules transferred from the fluid phase [25]. Table 2 shows a summary of supported metal nanoparticles synthesized by one-pot SFRD.

Ye *et al.* [87] used SFRD with H_2 reduction to synthesize Pd NPs by deposition and reduction of $Pd(hfa)_2$ on MWCNT support in $scCO_2$. SFRD was carried out at 3.47 ml high pressure stainless steel reactor at 80°C and 8.1 MPa for 5-10 min. TEM images showed a successful particle growth with a well-dispersion of spherical particles and the size in the range of 5–10 nm, anchored onto the external walls of MWCNTs.

Morere *et al.* [88] synthesized Pt, Ru, and Ni NPs supported on reduced graphene oxide (rGO) by SFRD. The metal complexes used for the synthesis were $Pt(cod)(CH_3)_2$, $Ru(tmhd)_2(cod)$, and $Ni(cp)_2$. Experimental conditions were 60°C, 13.0 MPa, 60°C, 10.0 MPa, and 80°C, 13.5 MPa for the Pt, Ni, and Ru experiments, respectively. The reductions were carried out by injection of H_2 to the supercritical medium at 80, 150, and 250°C for Pt, Ru, and Ni, respectively. Fig. 5 shows the TEM images of Pt, Ru, and Ni/rGO nanocomposites. In all the samples, a homogenous distribution of spherical particles on the surface of graphene sheets was observed. Fig. 5a shows TEM image of Pt/rGO with Pt loading of 2.3 wt%. A PSD in range of 2-7 nm and PS of 3.9 nm was observed for this sample, while larger Pt NPs ranging from 2 to 10 nm with the average size of 5.4 nm was observed in a sample with Pt loading of 6.4 wt% (Fig. 5b). Fig. 5.c and d show TEM images of Ru/rGO and Ni/rGO samples with metal loading of 5.2 and 1.0 wt%, respectively. The average size of Ni NPs was 15.1 nm, significantly higher than that observed for Ru NPs which was 4.4 nm. It was reported that generally larger PSs was obtained using SFRD compared to the samples reduced by H_2 at atmospheric pressure [88].

As described previously, the thermal reduction is another approach to reduce and decompose of the metal complexes by simply heating up the SCF instead of introducing a reducing agent. In the presence of a SCF, it has been observed that the metal complex can be converted to elemental metal at a lower temperature than that at atmospheric pressure. In the work carried out by Watkins and McCarthy [89], the $Pt(cod)(me)_2$ was converted to metallic platinum at 140°C, 26.5 MPa in scCO2, while the decomposition temperature of $Pt(cod)(me)_2$ as determined by differential scanning calorimetry was 208°C at atmospheric pressure.

Saquing *et al.* [90] obtained a similar results in preparation of highly dispersed platinum particles supported on a CA with an average pore size of 22 nm with high metal content. The impregnation was carried out at 18.6 MPa for 24 h. The temperature of the vessel was then increased to 135°C for thermal reduction, which also caused the pressure to increase to 31.0 MPa. The reduction in $scCO_2$ was continued for 6 h. It was observed that the PSs were 3.7 nm for the interior and 4.7 nm for the exterior microstructures. In these experiments almost all the platinum complex, $Pt(cod)(me)_2$ in the $scCO_2$ phase was adsorbed and subsequently converted to Pt in the CA substrate. For example, Pt/CA composites prepared with this method resulted in a loading of 60 and 73 wt. % Pt. For both composites, the impregnated Pt accounted for 97% of the

Table 2
Summary of SFRD studies in the literature on preparation of supported mono and bimetallic nanoparticles using $scCO_2$ without presence of a co-solvent: type of support and their physical properties, metal complex, and SFRD efficiency.

Metal complex Type	Melting point at ambient pressure (°C)	Support Type	Specific surface area (m^2/g)	Pore diameter (nm)	Pore volume (cm^3/g)	SFRD Max metal loading[a] (wt%)	Metal loading (wt%)	Reduction method	Efficiency (%)	Ref
Ru (tmhd)$_2$(COD)	N.S.	SBA-15	581	6.7	0.81	8.4	9.6	$scCO_2/H_2$	c	[92]
Ru(tmhd)$_2$(cod)	187-190	rGO	N.S.	N.S.	N.S.	8.0	5.1	$scCO_2/H_2$	63.8	[88]
Ru (tmhd)$_2$(COD)	N.S.	SBA-15	581	6.7	0.81	8.4	9.6	$scCO_2/H_2$	c	[92]
Ni(cp)$_2$	171-173	rGO	N.S.	N.S.	N.S.	5.9	1.0	$scCO_2/H_2$	16.9	[88]
Pd(hfa)$_2$•xH2O	N.S.	MWCNT	N.S.	20-30	N.S.	50	23	$scCO_2/H_2$	46.0	[93]
Pd(hfac)$_2$	N.S.	SBA-15	695	8.1	N.S.	17	13.7	$scCO_2/H_2$	80.6	[94]
Pt(cod)(me)$_2$	105	poly(4-methyl-lpentene	N.S.	N.S.	N.S.	2.85	2	$scCO_2$/ thermal	70.2	[89]
Pt(cod)(me)$_2$	105	Carbon Aerogel	670-740	4.1-21.1	0.78-3.63	62	60	$scCO_2$/ thermal	97.0	[90]
Pt(cod)(me)$_2$	105	SBA-15	N.S.	N.S.	N.S.	6.2	4.9	$scCO_2/H_2$	79.0	[95]
Pt(cod)(me)$_2$	105	rGO	N.S.[b]	N.S.	N.S.	9.8	6.4	$scCO_2/H_2$	65.3	[88]
Pt(COD)(me)$_2$	105	SnO_2 coated α-Al_2O_3	7.6	N.S.	N.S.	1.1	0.91	$scCO_2/H_2$	82	[96]
Pt(COD)(me)$_2$	105	γ-Al_2O_3	168	12.0	N.S.	N.S.	1.6	$scCO_2/H_2$	N.S.	[97]
Pt(COD)(me)$_2$, (Cp)Pd(allyl)	105, N.S.	SBA-15	705	6.0	N.S.	3.0	2.9	$scCO_2/H_2$	97	[98]
Pt(COD)(me)$_2$	88	TiO_2	59	N.S.	N.S.	6.8	4.2	$scCO_2/H_2$	61.7	[99]
Pt(COD)(me)$_2$	88	AL_2O_3	154	N.S.	N.S.	6.8	6.3	$scCO_2/H_2$	92.6	[99]
Pt(COD)(me)$_2$	88	MCM-41	893	N.S.	N.S.	6.8	6.2	$scCO_2/H_2$	91.2	[99]
Pt (cod)Me (n-C_3F_7)	25	Al_2O_3	168	N.S.	N.S.	4.8	3.6	$scCO_2/H_2$	75	[100]
Pt(COD)(me)$_2$ Cu(tfa)$_2$	105, 198	CA	750	19	3.6	46	34	$scCO_2/H_2$	74	[101]
Au(acac)(me)$_2$	81	BP2000	1350	4.3	N.S.	3.7	3.3	$scCO_2/H_2$	88.8	[102]
Au(acac)(me)$_2$	81	γ-Al_2O_3	154	17.5	N.S.	4.0	3.6	$scCO_2/H_2$	90.6	[102]
Au(acac)(me)$_2$	81	TiO_2	59	8.2	N.S.	3.6	3.2	$scCO_2/H_2$	88.8	[102]
Au(acac)(me)$_2$	81	β-cyclodextrin	1	0.8	N.S.	1.3	0.4	$scCO_2/H_2$	31.3	[102]
Co(cp)$_2$	178	MCM-41	1295	4.6	N.S.	6.63	4.34	$scCO_2$/ thermal	65.5	[103]
Co(cp)$_2$	178	Al-MCM-41	807	4.8	N.S.	6.63	5.1	$scCO_2$/ thermal	76.9	[103]

[a] Based on the initial amount of the metal prior to the impregnation
[b] N.S.: Not Specified
[c]EDX results showed a loading higher than the max metal loading

total Pt placed into the vessel in the form of Pt (cod) (me)$_2$.

The kinetics of the metal complex reduction reaction in $scCO_2/H_2$ has a direct effect on the PS of supported nanoparticles making one able to synthesize nanoparticles in a desired PS by changing the duration and temperature of the reduction process. Marre *et al.* [91] calculated the kinetic parameters and conversion rate of Cu(hfac)$_2$•H_2O in $scCO_2$/alcohol/H_2 at low temperatures assuming a first order reaction rate. They reported that the trend of PS obtained from TEM images was a function of residence time and temperature which could be directly linked to the kinetics constants of the reduction reaction. They also used a bimodal model to predict the PS as function of residence time and temperature considering two main steps in the model including the nucleation and particle growth by coagulation and coalescence. The predictions were in a good agreement with the experimental results showing kinetically controlled formation of supported nanoparticles.

2.4. Deposition approaches for bimetallic and multimetallic nanoparticles

Multimetallic NPs are composed of two or more different metals. Multimetallic supported NPs are both of academic and industrial interests as their properties are often different from either of the pure form of NPs. Bimetallic NPs (A_mB_n) can be generated with more or less controlled amount (m + n) and composition (m/n) with main mixing patterns as given in Fig. 6 [104].

The formation and growth of bimetallic NPs usually consist of a number of steps including nucleation, diffusion and growth. All these steps are usually governed by kinetic phenomena [105]. The degree of segregation/mixing and atomic ordering in A_mB_n bimetallic NPs depends on a variety of factors including relative strengths of A-A, B-B, and A-B bonds, relative surface energies of bulk A and B, relative atomic sizes, strength of binding to surface ligands (or surfactants) and specific electronic/magnetic effects [106]. The structure of the NP and degree of A-B segregation may also depend on kinetics of nucleation and growth for which the method and conditions of NP generation (type of particle source, metal complex, support, surfactant, temperature, pressure, etc.) becomes important. Supported multimetallic nanostructures have a wide variety of applications in nano biomedicine, catalysis, electrocatalysis, and sensing. In catalysis, they are used to not only enhance the performance but also for economic reasons [104].

Supported multimetallic NPs can be synthesized using SFRD by simultaneous deposition where the process is started with dissolution of two metal complexes simultaneously in $scCO_2$ followed by the same subsequent steps as in single component SFRD. Müller *et al.* [102] synthesized bimetallic silver-gold nanoparticles by simultaneous reactive deposition of Au(acac)me$_2$ and Ag(cod)hfac from $scCO_2$ on a variety of supports including BP2000 (carbon black), γ-Al_2O_3, TiO_2, and β-CD (β-cyclodextrin). The impregnation and reduction steps were carried out for 20 and 2 h, respectively, at the same condition of 80°C and 15.5 MPa used for all the SFRD experiments. The effect of support properties on mean particle size and distribution, particle structure and metal loading was investigated. With exception of β-CD, a correlation between the provided surface area of the supports and the mean PS of bimetallic

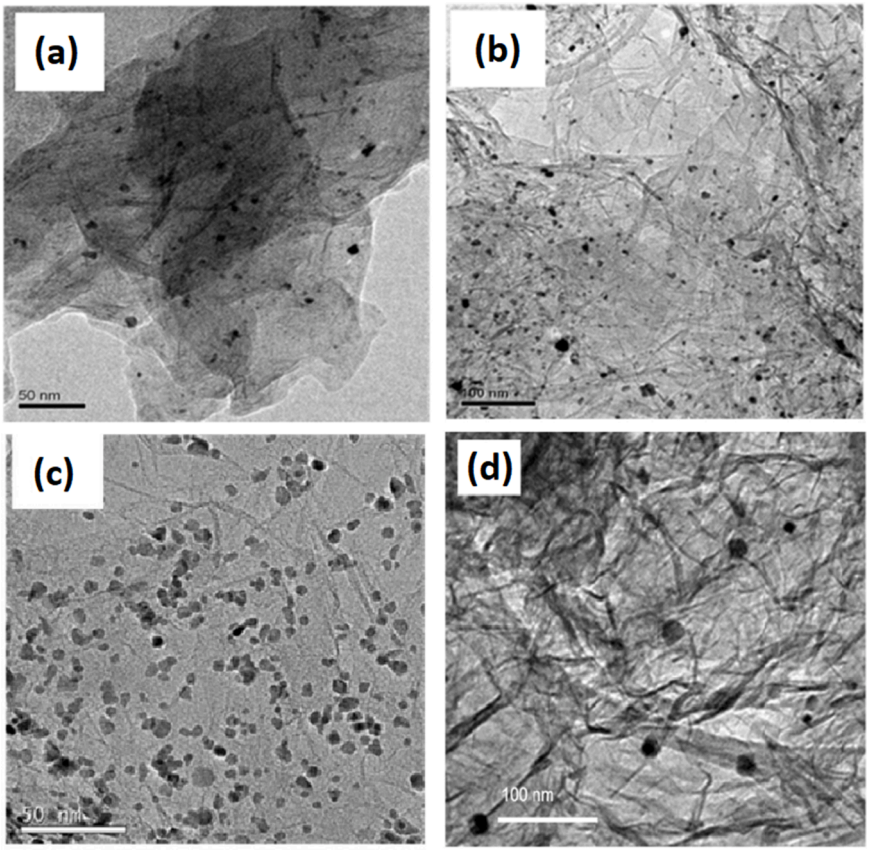

Fig. 5. TEM images of Pt, Ru, and Ni on rGO obtained by SFRD in $scCO_2/H_2$ (a) Pt 2.3 wt% (b) Pt 6.4 wt% (c) Ru 5.2 wt% (d) Ni 1.0 wt%. Reprinted from [88], ©2017, with permission from Elsevier.

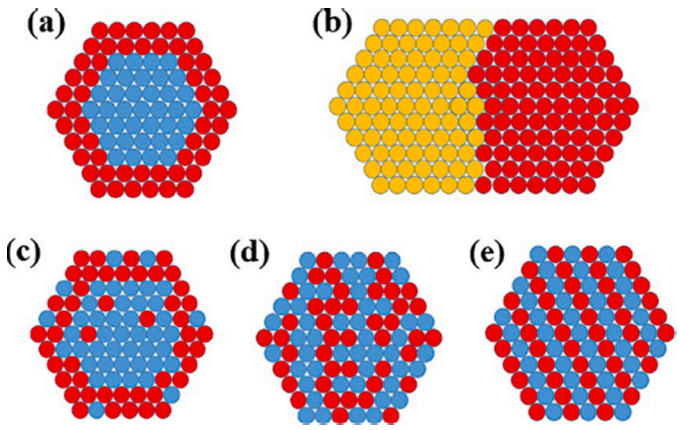

Fig. 6. Schematic representation of the examples of some possible configurations for bimetallic NPs: (a) core-shell, (b) segregated/Janus particle, (c) surface segregated, (d) disordered alloy, (e) ordered alloy. The illustrations display cross sections of the NPs showing an hypothetical face-centered cubic (FCC) (111) plane [104].

Ag-Au nanoparticles was observed from TEM images. PS values of 4.2, 17.8, 27.8, and 9.6 nm were obtained for BP200, ɣ-Al_2O_3, TiO_2, and β-CD, respectively. HAADF-STEM images together with EDXS line scan measurements showed that core/shell bimetallic nanoparticles with a gold core surrounded by an intermetallic AuAg phase with a composition of Au_1Ag_3 were successfully synthesized.

PtRu NPs supported on CNTs were prepared by Lin *et al.* [107] with PSs around 5–10 nm. The metal complexes $Pt(acac)_2$ and $Ru(acac)_2$ were simultaneously adsorbed on CNTs in $scCO_2$ at 200°C and 8 MPa. A small amount of methanol was added to deposition vessel. The metal complex conversion was conducted at 16 MPa and took 15 min with chemical conversion using H_2 as the reducing agent. Yen *et al.* [108] synthesized bimetallic Pt-Ru, Pt-Cu, Pt-Au, Pt-Pd, and Pt-Ni NPs supported on MWCNTs via simultaneous SFRD with $scCO_2$ at 10 MPa. Deposition temperature was 70°C for Pt-Au and 200°C for the others. Conversion of metal complexes were conducted by in situ chemical reduction with H_2 at 25 MPa. Resulting electrocatalysts had average PSs around 2.8–9.3 nm.

Using SFRD technology, Sánchez-Miguel *et al.* [95] was able to deposit Pt, Ru, Cu, and their bimetallic NPs onto SBA-15. Thecondition of the deposition step for preparation of bimetallic PtRu and PtCu was 80°C, 13.5 MPa and 60°C, 13.5 MPa, respectively. Temperature of the reduction by H_2 was higher than the deposition step and performed at 200°C. TEM images of these bimetallic nanocomposites showed a homogeneous deposition of the particles with broad PSD in an elongated form. In the case of PtRu a PS in range of 4-8 nm with average particle size of 5.7 nm was observed (Fig. 7a). The PS and PSD were slightly larger and broader than the ones obtained by reduction at atmospheric pressure and higher temperature (400°C). Rod-like particles with diameter of 7 nm and length of 18 nm with an average size of 10.7 nm was observed for PtCu bimetallic particles prepared by SFRD shown in Fig. 7b, which were again larger than the bimetallic PtCu particles obtained by reduction in atmospheric pressure. Generally, in case of SFRD, the adsorbed metal complexes are hydrogenated and solubilized in $scCO_2$ while in case of chemical reductions performed at atmospheric pressures, the adsorbed metal complexes are reduced and the decomposed ligands are removed. Thus, lower temperatures are required for reductions in SFRD technique as compared to the reductions performed at atmospheric pressures by H_2. It was claimed that in the case of bimetallic PtCu and PtRu, first Pt is reduced and sunsequently, the

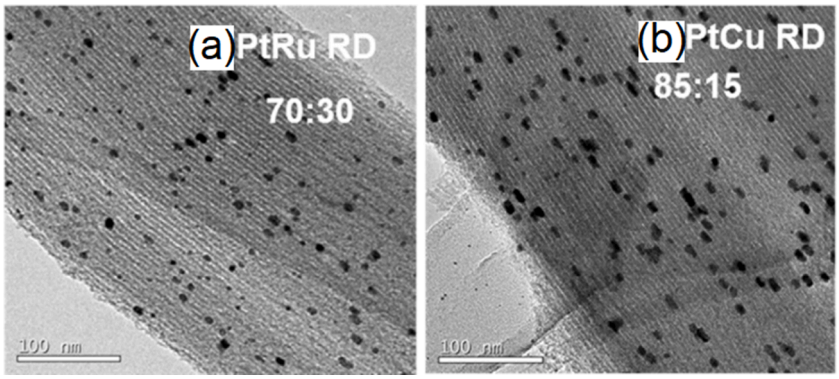

Fig. 7. TEM images of bimetallic PtRu (a) and PtCu (b) supported on SBA-15 prepared by SFRD in $scCO_2/H_2$. Reprinted from [95],©2017, with permission from Elsevier

reduced Pt particles catalyze the reduction of Cu and Ru metal complexes to their metal form. Comparison of the PS of bimetallic and monometallic samples prepared by H_2 assisted SFRD revealed that bimetallics were always larger than monometallic ones. This was due to higher metal loads and higher temperatures used in the reduction step of the bimetallic samples in comparison to those of pure Pt [95].

Barim *et al.* [101] utilized both thermal and chemical conversion techniques to synthesize bimetallic PtCu supported on CA or Vulcan. The materials were prepared by sequential and simultaneous deposition in $scCO_2$. For sequential deposition, first deposition of $Pt(cod)(me)_2$ onto the supports were carried out at 17.2 MPa and 80°C for 24 h. Subsequently, temperature of the vessel was raised to 135°C to perform a thermal reduction of the metal complex for 6 h. The prepared Pt/CA or Pt/Vulcan were then subjected to deposition of $Cu(tfa)_2$ at the same conditions used for Pt deposition. The conversion of adsorbed $Cu(tfa)_2$ to metallic form was carried out by injection of H_2 into the vessel until the blue color of the medium disappeared showing a complete conversion of the metal complex. In the simultaneous approach, the metal complexes were placed along with the supports in the vessel to perform the deposition at the same conditions with the sequential approach. The conversion step was completed thermally by increasing the temperature of the vessel to 135°C for 6 h followed by cooling down the vessel to 80°C and injection of H_2 until disappearing the blue color of the medium. The metal content results showed that the target molar ratio of Pt:Cu was obtained successfully by this method as evidenced by XRF measurements showing that SFRD is an effective and controlled route to synthesis supported bimetallic nanoparticles with a target molar ratio. The metal loading of Pt and Cu varied between 18.4 to 23.1 wt% and 13.4 to 18.7 wt%, respectively, depending on the deposition approach and support type. HRTEM images of the samples showed a homogenously distribution of the nanoparticles and a quiet narrow PSD with a mean PS less than 5 nm.

2.5. Depressurization and purification

As previously mentioned, one of the most important advantages of SFRD is to obtain well-dispersed NPs with controllable PS, metal loading and desired surface morphology. These properties can be tunable via changing operating and design parameters of SFRD. In the literature, changing these properties with the variations occurring in depressurization parameters was investigated in several studies. For instance, cupric nitrate in SCF successfully impregnated into SBA-15 with different PS, PSD via changing depressurization rates by Qiao *et al* [109]. Depressurization was conducted in various rates in the range of between 0.05 and 1.2 MPa/min by adjusting the the needle valve on the reactor while the other operating parameters were kept constant. After depressurization, loaded supports were examined via TEM and XRD. It was found that average PS decreased from 6.5 nm to 2.2 nm when the depressurization rate was increased from 0.05 to 1.2 MPa/min. Moreover, PSD of NPs on the support became narrower and monomodal as the depressurization rate was increased. XRD results show that the characteristic crystalline peaks of CuO became broader with increasing depressurization rate which indicated the average grain size of the dispersion phases decreased. Cu loading also increased with increasing depressurization. In another study, they compared the effects of depressurization rate and metal loading on morphology and dispersion of CuO NPs [110]. It was found that depressurization rate was a more important parameter than the metal loading amount for tuning the surface morphology. Moreover, the degree of dispersion of CuO NPs, and the controllability of PSD of CuO NPs were related to the critical concentration of the metal complex for nucleation at a certain depressurized rate. In another study, effects of changing depressurization parameters on PS and morphology were studied for Ag NPs [111]. It was found that PS decreased from 3 nm to 2 nm by increasing the depressurization rate from 0.1 MPa/min to 3 MPa/min. The results showed that the morphology of the dispersed phase was more uniform compared to slow depressurization rates.

After conversion of metal complexes to metallic nanoparticles on the surface, some of the decomposition products may adsorb on the surface and may need to be removed from the surface. In SFRD, this can be carried in the same vessel using supercritical extraction (SCE) [112]. For instance, Yousefzadeh *et al.* used SFE to remove copper(II)trifluoroacetylacetonate ($Cu(tfa)_2$) and other impurities on the substrate after supercritical ion exchange process [113]. These physically adsorbed impurities were successfully removed from the substrate by passing pure $scCO_2$ through the vessel at 24.1 MPa and 80 °C.

3. Producing thin metallic films via SFRD

A metal layer on a substrate with a thickness ranging from a nanometer to several micrometers is called as thin metal film. In contrary to metal NPs, the preparation of thin films via SFRD has been reported only by a few groups. In the literature, Watkins and co-workers conducted most of the seminal works in SFRD of thin films [114–116]. Following their studies, high quality thin films of various metals and metal oxides including Cu, Co, Ni, Mo, Pt, Pd, Ru, Ag, Au, Rh, Ir, hafnium oxide, zirconia, ceria stabilized zirconia, ceria, titania, tantalum oxide, niobium oxide and bismuth oxides were obtained on a wide variety of substrates using SFRD [22,23,117-124].

Compared to the other methods such as sol-gel, CVD, sputtering, electrochemical deposition to produce thin metallic films, SFRD has several advantages to produce a thin metallic layer such as processing at low process temperatures, enabling conformal deposition of thin films in confined geometries with high aspect ratios and order of magnitude higher solubility than CVD [26,125]. Moreover, dissolution of by-products in SCFs results in a good film quality and dissolution of most

common reducing agents such as H_2 and alcohols makes this process attractive.

Majority of SFRD studies to prepare thin films are conducted in cold-wall reactors since the metal complex is deposited only on surface of heated support. The support is heated directly either by induction or by radiant heating while the rest of the reactor remains cold or colder similar to the CVD processes in cold-wall reactor [27]. The schematic demonstration of a cold-wall rector in the batch mode which was used by Watkins group is given in Fig. 8 [126]. First, support is primarily placed in the reactor and metal complex is fed into the reactor. Reactor is equipped with a band heater to heat the reactor wall. The pedestal heater allowing the selective heating of the substrate during the SFRD process while keeping the reactor wall at a lower temperature. Due to this temperature difference between the heating stage and the reactor wall, natural convection occurs in cold-wall reactors in batch mode.

Reactor operated in continuous mode is given in Fig. 9 which was developed by Watkins *et.al* for preparation of thin metal films within porous substrates. In this particular design, resistive heating elements heat the reactor and precursor feed. The syringe pump reservoirs are heated with a water/glycol heating jacket. The substrate and a polymer barrier divide the reactor into separate precursor and H_2 chambers. Similar to the batch reactors, syringe pumps are used to pumping gases from gas tanks to the vessel at controlled rates. Pressure drops across the support and polymer is minimized by a connection between the metal precursor and H_2 side outlets where the streams mix. The effluent stream passes through a carbon bed to adsorb products in the fluid phase. A backpressure regulator is used to control the system pressure [127]. In another study, the temperature profile with fluid flow pattern in the cold-wall reactor both in batch and continuous modes were explored [128]. First, the effects of the reactor clearance above the heater on the thermal profiles were studied. A thermocouple was inserted into a thermowell from the side wall and moved to the middle of the vessel to measure the temperature from different locations along the length of the reactor. They examined the temperature differences 0.2 and 0.4 mm above the stage for two different clearances as 51 mm and 12.7 mm. The initial temperature of the stage was 127°C and then it was set to 225°C. They observed that in the reactor having a large clearance, temperature gradient was uniform. Therefore, they reported that the cold-wall reactor with low clearance is not suitable design for thin film deposition since changes in the temperature gradient is not the desired condition for the film deposition.

The reaction mechanism and kinetics of film forming process were investigated by Watkins and co-workers. In their study, Cu film deposition on TiN-coated Si with the assistance of H_2 was conducted in a cold wall reactor in batch mode. At the beginning of the process, the substrate was fixed on the heating stage and a desired amount of $Cu(tmod)_2$ as a metal complex was loaded to the reactor. After sealing, the reactor was purged with CO_2 while the temperature was set to 60°C. Subsequently,

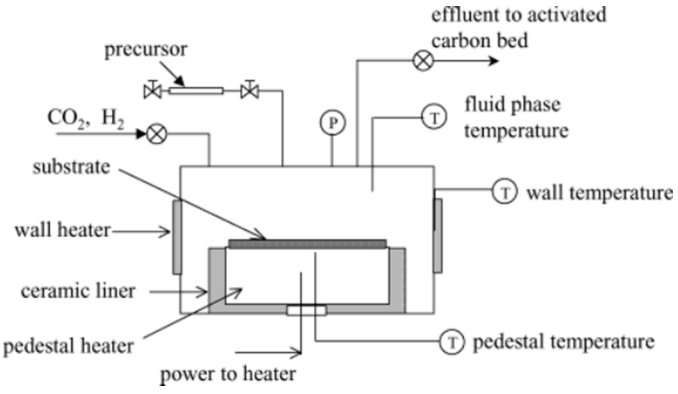

Fig. 8. Cold-wall reactor design in batch mode. Reprinted from [126], ©2004, with permission from American Chemical Society.

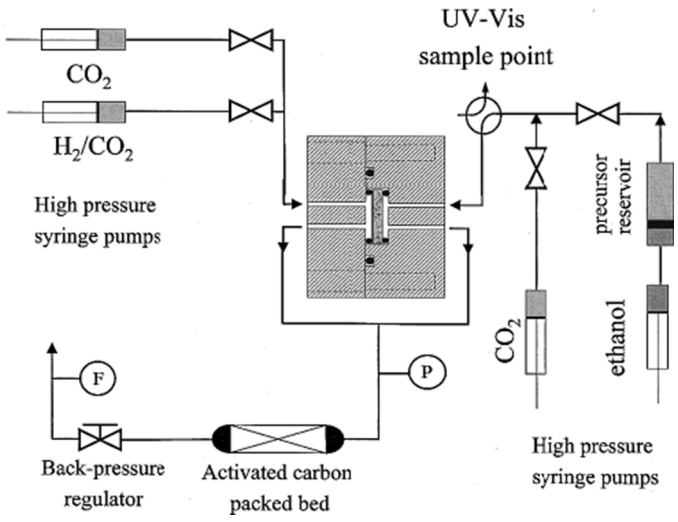

Fig. 9. SFRD setup in continuous mode for preparation of thin metal films within porous substrates. Reprinted from [127], ©2001, with permission from American Chemical Society.

CO_2 was introduced to the vessel at various pressures between 10 and 13.8 MPa. After complete dissolution of the metal complex, vessel was filled with H_2 at different amounts. Deposition was started by turning the heating stage. The deposition temperatures which were between 220-270°C was obtained in 40 s. When the stage temperature was decreased to 200°C in 10 s, reaction was stopped. Overall process time was recorded as 5 minutes. The growth rate was reported between 5 to 35 nm/min within the temperature range of the process. In this process, the mechanism was proposed as as adsorption of metal complex, dissociation of the ligands for Cu formation, adsorption and dissociation of H_2 onto the surface, protonation of ligand from adjacent surface adsorbed ligand and hydrogen atom to form volatile by product and hydrogenated ligand, desorption of by product and diffusion of by product into $scCO_2$ solution. The growth rate of the Cu film was successfully described by Langmuir-Hinshelwood-type rate expression. The concentrations of the metal complex, hydrogen, and byproducts were the variable of the rate equation along with temperature. This study shows again the importance of understanding the kinetics of the different steps of a SFRD process to be able to adjust the physical properties of the prepared nanostructured materials by tuning the synthesis condition [114].

Watkins group also utilized another reaction mechanism in the preparation of metal oxide films which is surface-selective hydrolysis of metal complex in $scCO_2$ [129,130]. They successfully deposited cerium (CeO_2), hafnium (HfO_2), titanium (TiO_2), niobium (Nb_2O_5), tantalum (Ta_2O_5), zirconium (ZrO_2), and bismuth (Bi_2O_3) oxides films on silicon wafer via hydrolysis of metal complexes. To initiate the metal complex decomposition by hydrolysis leading to film deposition, stage temperature was increased quickly up to 300°C. It was shown that the water content in $scCO_2$ with the process temperature governed the hydrolysis of metal complex. Thus, increasing water content led to the metal complex decomposition by hydrolysis and high deposition rate was obtained.

The effects of process parameters and support and metal complex properties on film quality and thickness have been investigated. In a study conducted by Cabañas *et al.*, the thickness of the Au films varied between 90 to 400 nm depending on the support type and the metal complex loading [131]. They deposited Au films on metal, ceramic, and polymer supports separately via H_2 assisted SFRD in cold-wall and hot-wall reactors in a batch mode. At a low temperature of 60°C, deposition was selective for metal surfaces while at a high temperature as 125°C, Au deposited readily on all surfaces studied. Hunde and Watkins investigated the effects of temperature on film thickness [126].

In their study, Co film was applied on uncoated SiO_2 and TaN or TiN coated SiO_2 in $scCO_2$ with the assistance of H_2 using cold-wall reactor in batch mode. Compared with the previous methods, H_2 was introduced after the stage was heated to specified temperatures which were 285 and 320°C. The film thickness was measured as 150 nm at 285°C whereas it was 680 nm at 300°C after 30-45 min deposition which indicated that even a small increase in temperature leads to much higher growth rates of the Co films. Changing film thickness with the deposition time was investigated by O'Neil and Watkins via depositing Ru film on both SiO_2 and tantalum coated Si wafer with H_2 assisted $scCO_2$ in a cold-wall reactor [129]. Film depositions were performed at different pressures between 20-25 MPa with various stage temperatures of 175 to 300°C. They found that at the same temperature, the film thickness obtained at 5 minute was almost half of thickness of the film obtained at 30 minutes. It can be attributed that the deposition was completed earlier than 30 minute and obtained film thickness did not give adequate information about reaction kinetics. In their another study, the effects of humidity and addition of the water to dry CO_2 on metal oxide thickness on Si and etched Si supports were investigated [129]. Support temperature was varied between 250 and 300°C in a cold wall reactor for the deposition of metal oxides which were CeO_2, HfO_2, TiO_2, Nb_2O_5, Ta_2O_5, ZrO_2, and Bi_2O_3. As an oxidizing agent H_2O was used and the process pressure was varied between 11-20 MPa whereas film growth took 30 min. To eliminate the mixed oxide state of the films, calcination was performed at 800°C for 1 h for TiO_2 and Bi_2O_3 while it took 6h for other metal oxide films. A high film thickness of 58 nm was obtained when trace amount of water was introduced the system compared to the case when dried CO_2 was used where 21 nm of film thickness was obtained. Increasing water concentration from 0.11 mmol to 0.28 mmol led to an increase in film thickness from 216 nm to 247 nm while further increase in water content caused a reduction in the film thickness. Bassat *et al.* studied changing film thickness and micro/nanostructure of the films with the variations occurring in molar ratio between humidity in CO_2 and metal complex [132]. SFRD of undoped ceria films on top of both sides of yttria-stabilized zirconia (YSZ) was conducted in a cold wall reactor via hydrolysis of tetrakis(2,2,6,6-tetramethyl-3,5-heptanedionato) cerium. The stage temperature was set to 300°C and an annealing was conducted in air at 400°C. Uniform, conformal and crystalline CeO_2 films with a thickness ranging from 20-200 nm were obtained in 30 minutes in humidified $scCO_2$. Increasing H_2O:Ce complex molar ratio from 0 to 12 was stated to favour the metal complex hydrolysis which led to thicker, smoother and denser films. In their next study, the authors showed that the changing pressure did not affect the deposited film morphology and longer deposition time up to 3 h led to an increase in the thickness of the film without changing the film morphology [130].

Zhao *et al.* deposited TiO_2, bismuth oxide (Bi_2O_3), bismuth titanate (BIT, $Bi_4Ti_3O_{12}$) films on SiO_2 coated Si wafers in a cold-wall reactor in a continuous flow mode [133]. As Ti and Bi sources, $Ti(O\text{-}i\text{-}Pr)_2(tmhd)_2$ and $Bi(ph)_3$ were used, respectively. At the beginning of the process, excess amounts of metal complex were loaded to the hot-wall reactor to dissolve metal complexes at 50°C and filled with CO_2 at 10 MPa. $Bi(ph)_3$ was dissolved in $scCO_2$ in the presence of O_2 whereas for deposition of BIT, O_2 was not used since $Ti(O\text{-}i\text{-}Pr)_2(tmhd)_2$ has oxygen atoms. A $scCO_2$ stream saturated with metal complexes were diluted with pure CO_2 before delivery to the cold-wall reactor. It was reported that maximum film thickness which was 35 nm was obtained when the Ti:Bi concentration ratio in $scCO_2$ was 0.3. Kondoh *et al.* also deposited Ni-Pt alloy thin films on TiN/SiO_2/Si substrates through hydrogen reduction of $Ni(hfac)_2$ and $Pt(hfac)_2$ metal complexes in $scCO_2$ in a continuous flow mode [134]. The results indicated that the deposition rate of the Ni-Pt thin alloy films decreased with increasing Ni content and gradually increased as the metal complex concentration was increased. The deposited films were single-phase polycrystalline Ni-Pt solid solution and they exhibited smooth, continuous, and uniform distribution on the substrate for all elemental compositions. Fernandes *et al.* carried out SFRD for another porous support which was alumina and a continuous Pd film was deposited on both the surface and at controlled depths of pores at 60°C [127]. Pd films between 2 and 80 μm thick at specified depths between 80 and 600 μm as measured from the metal complex side were successfully deposited.

As opposed to conventional batch and continuous processes, Le Trequesser *et al.* used a cyclic co-deposition process of YSZ thin films on Si wafers using $scCO_2$ with 300°C stage temperature, and 15-20 MPa pressure [135]. Both zirconium (IV) hexafluoro acetylacetonate and yttrium (III) hexafluoro acetylacetonate complexes were stated to undergo a hydrolysis reaction for yttria and zirconia film formation, respectively. In each cycle, the mixed metal complex solution in CO_2 was introduced to the reactor and then purged following a short reaction interval which resulted in considerable uniformity improvement in film composition. Therefore, a precise control of stoichiometry was attained, and the resulting film had a uniform composition. Moreover, under same conditions with conventional batch processes, cyclic deposition provided thicker films since higher reaction rates are obtained in the cyclic process via driving the reaction to the product side with refreshing water concentration in each cycle.

4. Electrochemical deposition in supercritical fluids

Electrodeposition is a widely used materials-deposition technology with a number of unique features, in particular, the efficient use of starting materials, conformal, and directed coating. The properties of the solvent medium for electrodeposition are important on capability of the technique. Supercritical fluids have unique properties which give a wide range of advantages for chemistry in general, can be an alternative solvent medium to commonly used organic conductive solutions. Low viscosity of SCF can lead to enhanced mass transport to and from the electrode surface [136]. Good pore penetration allows deposition of small particles. A lack of surface tension allows electrodeposition onto fragile substrates. Moreover, presence of a range of SCFs with high chemical stability enables different materials to be suitable for electrodeposition [137].

In 1986 McDonald *et al.* [138] conducted deposition of the Cu/Cu (I)/Cu (II) system in $NaSO_4$ and KCl solutions under near critical and supercritical conditions. Electrochemical characterization was done with cyclic voltammetry and diffusion coefficient is determined. Ke [139] carried out electrodeposition of a range of metals from $scCO_2$/acetonitrile, and supercritical difluoromethane. They deposited 3 nm diameter copper nanowires in mesoporous silica templates on ITO. Ke *et al.* [140] investigated the electrodeposition of Ge using Ge(II) and Ge (IV) compounds as reagents from liquid CH_3CN and CH_2F_2 and $scCO_2$ containing as a co-solvent CH_3CN ($scCO_2$) and supercritical CH_2F_2 ($scCH_2F_2$). They found deposition of Ge obtained using $GeCl_4$ in liquid CH_2F_2 and $scCH_2F_2$ was promising. Consistent values of reduction currents with mass transport limited was obtained. Also, amorphous elementary Ge was electrodeposited from $scCH_2F_2$. Bartley *et al.* [141] investigated electrodeposition of silver from $scCO_2$/acetonitrile using five different silver precursors. Among these precursors, they found $[Ag(CH_3CN)_4][BF_4]$ the most suitable since they were able to deposit silver nanowires into anodic alumina templates with sizes down to 13 nm and good quality silver films onto macroelectrodes. Bartley *et al.* described a versatile electrolyte bath for the deposition of elemental Ga, In, Ge, Sn, Sb, Bi, Se, and Te from $scCH_2F_2$ and the resulting deposits were characterized with SEM, energy-dispersive X-ray analysis, XRD and Raman spectroscopy. They concluded that wide range of materials will be accessible for electrodeposition with this electrolyte system [142]. In their later studies, Bartley *et al.* explored deposition of wires with small size diameters using SCFs. They obtained tellurium nanowires (TeNW) of nominal size range 13 nm to 55 nm diameter [143] and tens of micrometers in length and Sn Nanowires with sub 7 nm diameter [144] and characterized their structure and stability.

Chuang *et al.* fabricated copper nanowires inside Anodic Aluminum Oxide templates using supercritical and post-supercritical electroplating

technique. They achieved smallest grain size with supercritical electroplating followed by the post-supercritical electroplating and then the traditional electroplating process [145]. Later, they applied ultrasonic agitation on $scCO_2$ copper electroplating. They reported that applying ultrasound to $scCO_2$ electroplating process can significantly improve the mechanical properties of the coating [146]. Moreover, Chuang et al. presented a novel ultrasound-assisted supercritical argon (scAr) electroplating process with no additives to produce copper metal coatings [147]. The resulting coatings showed improved mechanical and corrosion behavior compared to the coatings produced by conventional or silent scAr processes. They also adjusted electroplating parameters such as temperature, pressure and current density to optimize the process and characterized mechanical, electrical and corrosion properties [148].

5. Supercritical Ion Exchange

Ion exchange is basically a reversible chemical reaction by which ions present on the surface of solid phase are exchanged with the like charge ions present in the solution surrounding the solid material. It was shown that the reaction can also occur between two solid materials. The former one is called aqueous ion exchange (AIE) and the latter one is called solid state ion exchange (SSIE). Recently, Erkey research group developed a new route of ion exchange called supercritical ion exchange (SCIE) to prepare copper exchanged zeolites using $scCO_2$ [113]. The method consists of the dissolution of a copper complex in $scCO_2$ followed by diffusion into the zeolite pores from the fluid phase, adsorption on the zeolite surface, and ion exchange with Brønsted acid sites. Reaction of copper complex with the Brønsted acid sites in the zeolite structure led to forming of copper species in the solid phase and trifluoroacetylacetone in $scCO_2$ medium. Here in this method, the metal complex is converted to its metallic form via ion exchange reaction in which the required H_2 molecules are provided by the extra framework protons of the zeolite structure and the metal atoms are chemically bonded to the zeolite framework. Therefore, the method is a kind of SFRD since it consists of all the steps of a typical SFRD including dissolution, adsorption, reduction of the metal complex, and depressurization. Furthermore, the support material has a porous structure like the ones are used in a typical SFRD. The final material consists of different copper species including mono, di, tri-coppers and copper clusters supported on the zeolite. A brief explanation of the experimental procedure and experimental evidence for occurrence of the ion exchange reaction are given in the following.

Pellets of mordenite zeolite with extra framework protons (H-MOR which is obtained by the calcination of NH_4-MOR in an inert atmosphere) together with the copper(II)trifluoroacetylacetonate were placed in a high pressure vessel. First the air in the vessel was purged out by passing CO_2. Subsequently, the vessel was heated up to a desired temperature above the critical temperature of CO_2. It was then pressurized to a desired pressure to obtain $scCO_2$ medium. After dissolution of the metal complex and a certain period of ion exchange, fresh $scCO_2$ was fed to the vessel to perform SFE to remove those of physically adsorbed metal complexes on the solid surface and the products of the ion exchange reaction present in the fluid phase. The results obtained from characterization tools such as NMR, XRF, FTIR and visual observations demonstrated that an ion exchange reaction occurred between copper complex and H-MOR in $scCO_2$. The photograph of the high-pressure vessel during the dissolution and the reaction of CuL_2 with H-MOR in $scCO_2$ (at 27.58 MPa and 80°C) is shown in Fig. 10a and b. The initial color of the solution was blue which was the color of solution when CuL_2 is dissolved in pure $scCO_2$ at these conditions. The color of the solution gradually changed from blue to yellow with time. The yellow color of the solution could be attributed to the formation of trifluoroacetylacetone ($C_5H_5F_3O_2$, i.e. HL) since the color of HL in $scCO_2$ in presence of H-MOR zeolite was also yellow at the same temperature and pressure.

The comparison of ^1H NMR spectra of the fluid phase during the ion exchange and pure trifluoroacetylacetone showed that chemical shifts of the peaks associated with CH enol form (5.867 ppm) and CH_3 moiety (2.160 ppm with the small peak at 2.187 ppm) observed in the sample taken from the high-pressure fluid phase were in very good agreement with the ^1H NMR spectrum of pure trifluoroacetylacetone as shown in inset of Fig. 11.

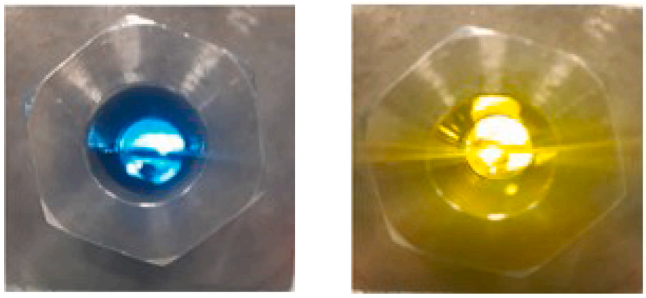

Fig. 10. high pressure vessel, at the start of SCIE (a), after a certain time of SCIE (b), pressure and temperature were the same for all experiments (27 MPa, 80°C).Reprinted from [113], ©2022, with permission from Elsevier

Therefore, Cu-MOR and trifluoroacetylacetone (HL) were the products of the ion exchange reaction as expected based on the following ion exchange reaction:

$$CuL_{2(scCO_2)} + 2HZ_{(s)} \leftrightarrows CuZ_{(s)} + 2HL_{(scCO_2)}$$

where, L is trifluoroacetylacetonate ligand and Z is the zeolite framework with unit negative charge. According to the reaction, two protons coordinated oxygen atoms linked to Al atoms in the framework of H-MOR (Brønsted acid sites) exchanged with one copper ion of CuL_2. In addition, FTIR spectra of treated samples illustrated that the intensity of Brønsted acid site peak decreased in Cu incorporated samples compared with parent H-MOR sample pointing out that coppers were exchanged with the H^+ protons of the Brønsted acid sites. Moreover, comparison the results of XRF analysis of the samples obtained after SCIE and after the subsequent SFE steps revealed that Cu loading of the samples before

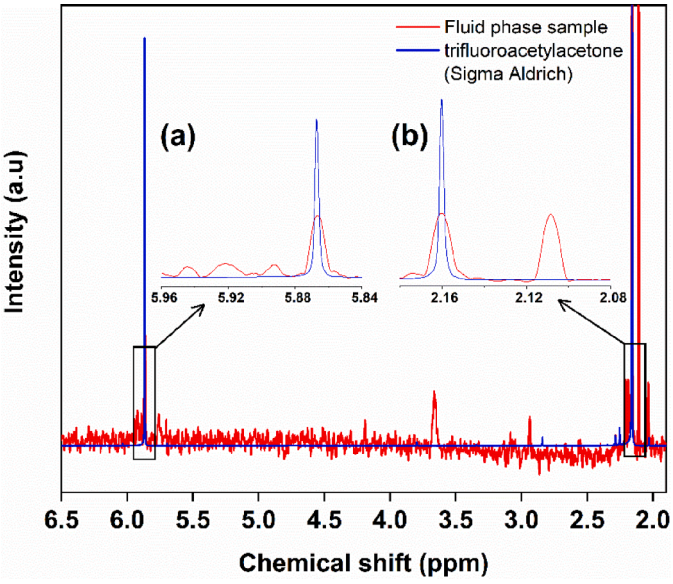

Fig. 11. ^1H NMR spectrum of fluid phase sample taken in $CDCl_3$ at t=5h of SCIE of CuL_2 with H-MOR at 80 °C and 27.58 MPa for the synthesis of Cu-MOR_S with 1.5 wt%. (inset (a): zoom-up region between chemical shifts of 5.84 to 5.96 ppm. inset (b): zoom-up region between chemical shifts of 2.14 to 2.18 ppm). Reprinted from [113], ©2022, with permission from Elsevier

and after SFE was identical, indicating that the exchanged Cu atoms were chemically bonded to mordenite surface and were not in any other form such as physically adsorbed metal complex which would be extracted.

The cation ion exchange isotherm obtained at 80°C and 27.6 MPa showed that the maximum copper loading never reached to the total cation exchange capacity of the zeolite indicating that the SCIE is a selective ion exchange process (solid phase equivalent fraction does not go to unity). This showed that, at equilibrium, only a certain fraction of surface sites is exchanged in the SCIE process, probably due to the mass transfer limitations caused by the microporous structure of H-MOR preventing the copper complex to reach all exchangeable sites. Copper exchanged zeolites are extensively used in a variety of applications including catalysis [149–151], adsorption [152,153] and sensing [154, 155]. Among these, NOx abatement using the NH_3 Selective Catalytic Reduction (NH_3-SCR) process and step-wise direct conversion of methane into methanol (sDMTM) make use of the Cu-exchanged zeolites as catalysts which have recently become the state-of-the-art to both industry and academy due to high reactivities and selectivities. The structure of copper species formed during these reactive processes play an important role to determine the catalyst performance, which is generally affected by the zeolite structure, synthesis method, and the catalytic process conditions. The behavior of the cation ion exchange isotherm obtained by SCIE points out to the occurrence of selective ion-exchange during SCIE which could result in the formation of active Cu species with selective speciation during the sDMTM [113].

6. SFRD scale up approaches

The great potential of SFRD has been shown via lab-scale investigations of thin film and supported NPs preparations in sections 3 and 4. Commercialized SCF based processes such as extraction of hops and spices, decaffeination of coffee and tea, extraction of flavours, fragrances, and aromas from plants, wood impregnation, leather tanning, and textile dyeing may inspire the researchers and engineers working on SFRD in the lab-scale to design and operate the process in an industrial scale to prepare supported metal nanoparticles and films. In this section, first a brief overview of the SCF based industrial-scale technologies is given and then the suggested process design of a large scale SFRD plant is explained.

The first large-scale industrial solvent extraction plant was built in 1942 by Mallinckrodt Chemical Company for production of tons of uranium by selective extraction of uranyl nitrate by ether from aqueous solutions. In the 1950s and early 1960s, solvent extraction was introduced as a separation and purification process in numerous chemical and metallurgical industries. In 1978, first commercial decaffeination of green coffee beans via SFE was performed in Germany [156]. In the 1980s and 1990s, significant number of studies have been reported in the literature on SFE of different organic compounds from various matrices with the objective of replacing commercially available organic solvents. Today, about three hundred plants are operated at commercial scale mainly dedicated to extraction of hops and spices, decaffeination of coffee and tea, extraction of flavours, fragrances, and aromas from plants and producing aerogels [22]. These plants are distributed mainly in Europe, USA and Japan. Table 3 lists some of the commercialized SFE plants together with some extractor sizes and demonstrates the wide acceptance of SFE technology at industrial scale [9]. Some of these plants particularly hops, tea and coffee have a production capacity of 15-30 million kg per year.

Commercial plants employing SFE technology were built for batch extractions. At present, about 100 different types of extractors larger than 1000 litres have been designated for different industrial plants [157]. For instance, Amar Company manufactured 1000 L batch SFE reactor which may be operated at a pressure up to 350 bar and a temperature up to 100°C. Feed capacity of the reactor is 2400 kg/day. In their design, the raw material in powder form is fed to the extractor. The

Table 3
Examples of commercial supercritical extraction plants [9].

Coffee decaffeination	Jacobs Suchard, Bremen, Germany (360lt)
Hops extraction	Hopfenextraktion, HVG, Barth, Raiser & Co. (200lt + 500lt) SKW Trostberg, Munchsmunster, Germany (650lt) Natal Cane By-Products Ltd., Merebank, South Africa (1000lt) Barth & Co., Wolnzach, Germany (4000ltx5)
Color extraction—Red Pepper	Mohri Oil Mills, Japan Fuji Flavor, Japan (200lt + 300lt + 300lt) Natal Cane By-Products Ltd,. Merebank, South Africa (200lt) Hasegawa Koryo, Japan (500ltx2)
Flavors/aromas/spices	Guangxia Toothpaste, China (500ltx3, 3500ltx3, 1500ltx3) Flavex, Rehlingen, Germany (70lt) Raps & Co., Kulmbach, Germany (500ltx3) Shaanxi Jia De Agriculture Eng. Co., Ltd., China (500ltx2)
Nicotine extraction	Philip Morris, Hopewell, Virginia Nippon Tobacco, Japan (200lt)
Solvent Extraction	Aspen Aerogels, ABD.

liquid CO_2 from the tank is precooled by passing it through the precooler. This precooled liquid CO_2 is then pressurized above the critical pressure and is then heated above the critical temperature by passing it through preheater. Subsequently, $scCO_2$ enters the extractor in which the raw material is loaded. $scCO_2$ dissolves substances on the basis of solubility, depending on operating conditions. Afterwards $scCO_2$ with soluble extracts enters the separators where the pressure and temperature are reduced sequentially so that solubility decreases which lead to precipitation of extract in the separators. Finally, free CO_2 without any traces is recycled back to the CO_2 tank via condenser. $scCO_2$ based industrial scale impregnation plants has been developed for wood impregnation, leather tanning, and fabric dyeing processes in the last two decades. Dissolved molecules in $scCO_2$ such as fungicides, polymers, and dyes diffuse into porous and natural materials, such as wood, cork, leather, and fabric fibers [158]. Woods are impregnated by organic fungicides to protect them from deterioration by the environmental exposure. A large-scale batch vessel was constructed in Denmark by NATEX company to impregnate fungicides into wood using $scCO_2$ which was the world's first commercial supercritical wood treatment unit [159]. An unharmful organic fungicide is used in this technology. The process provides a superior penetration leading to an impregnation that cannot be obtained via conventional routes. Figs. 12 and 13 show the process schematic and receiving-handling systems along with the high pressure vessels. The treatment vessels with a length of 7 to 25 m is charged with wood packages. The impregnation is started after pressurizing the vessel with CO_2 up to 15 MPa and heating to 40-60°C. The method was successfully replaced with the conventional wood impregnation method based on heavy metals or organic solvents. Much shorter impregnation time, no drop-off or evaporation, and no change in the wood or in moisture content were the advantages of this process. The plant has an annual capacity of 60000 m^3 with cycle time of 2-5 h and CO_2 recovery of 96%.

Leather tanning by SCF is another process that is commercialized in the last decades. The conventional route involves a pre-treatment of hides by acids in water bathes in presence of salts followed by adding the tanning agent which is chromium-based. Collagen molecules are linked to each other through a chemical reaction with the tanning agent which is triggered by increasing the pH value. High costs for recycling, enormous environmental problems, and long duration of the process are the main disadvantages of the conventional rout. Tanning time is decreased from 30 h for the conventional rout to 5 h when $scCO_2$ is used. In addition, using $scCO_2$ leads to an increased amount of impregnated chromium with a moderate impregnation rate as compared to the conventional technique [158]. In this process, the dried hides are placed in a

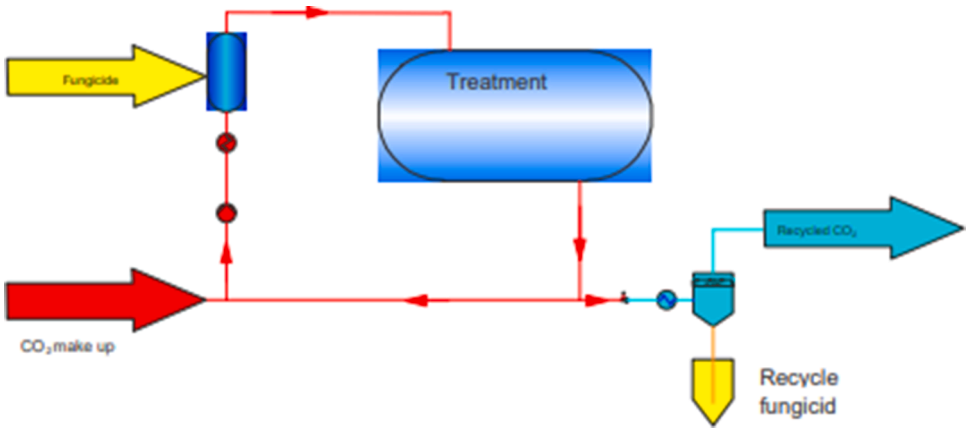

Fig. 12. Schematic visualisation of the supercritical wood treatment process [159].

Fig. 13. The world's first commercial supercritical wood treatment plant: receiving and handling system [159].

rotating autoclave followed by pumping the aqueous chromium sulphate (tanning solution) into the vessel which is fully adsorbed by the hides. The vessel is then pressurized with CO_2 to accelerate the diffusion of tanning agents into the microstructure of the hides and formation of oligomers. Pressure, and temperature range of the process is kept between 0.3 to 10 MPa, and 30-40°C, including liquid or supercritical phases of CO_2. Based on the lab and pilot scale studies, a plant with 3 batch rotating tanning drum with a quick closure was designed to operate at 3 MPa. Fig. 14 shows one of these rotating drums with volume of 15 m^3 designed for treatment of 10 ton hide per shift. It was shown

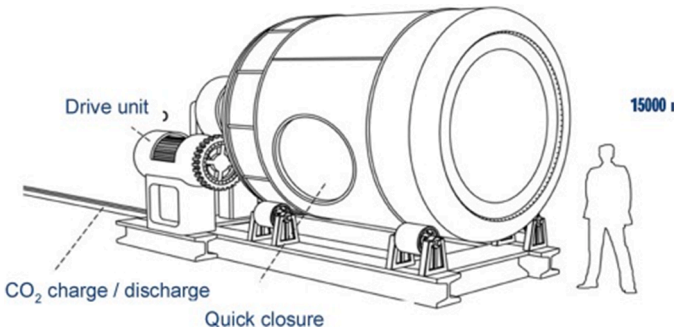

Fig. 14. Large scale rotating drum for CO_2-intensified hide tanning. Reprinted from [160], ©2018, with permission from Elsevier.

that the convective mass transfer is improved in the large drums caused by the rotating mechanism which in turn results in reducing the time of process to 3.5 h [160].

SFRD can also be carried out in a large-scale batch mode similar to wood impregnation and leather tanning. Recovery of CO_2, separation of CO_2 from the byproducts such as hydrogenated ligands, extraction of remained metal complex from the deposition vessel and process lines, and providing a desirable external mass transfer would be the main challenges for design of such a large scale SFRD process. Fig. 15 shows the schematic view of the suggested large scale SFRD setup working with one hot-wall deposition vessel. The number of vessels and separation units can be increased in a parallel mode. The support material is placed inside a rotating basket fixed on the mixer stem to provide a desired external mass transfer. After loading the support and metal precursor(s), the vessel is heated to the desired temperature followed by charging with CO_2 up to a certain pressure. The chemical reduction by injection of H_2 is performed after a certain time of adsorption by compressing and injection of pure H_2 into the deposition vessel at a desired molar ratio of CO_2/H_2. Thermal reduction can also be performed in this setup via increasing the temperature of vessels. After a certain time of reduction, the vessel is depressurized slowly. The outlet stream containing CO_2, unreacted metal complex, and by products is sent to a solid separator to remove solid compounds. The gas phase stream obtained from the top of the separator is pressurized and sent to an adsorption column using a compressor to remove by products such hydrogenated ligands formed during the reduction step. Pure CO_2 in a gas phase obtained from the adsorption column is recycled into the liquid CO_2 feed tank. Prior to the next material synthesis, the vessels are flushed with excess $scCO_2$ to remove the remained compounds. In this step, the outlet stream of the vessels is also subjected to the separation processes to recycle the excess CO_2. Performing SFRD in a continuous mode would be difficult since it requires charge and discharge of solid materials including metal complexes, supports, and final product during the process.

7. Applications

7.1. Catalysis

SFRD has been widely used to prepare various supported metal NPs as the catalysts for mainly hydrogenation and oxidation reactions. Table 4 summarizes the literature studies in terms of type of catalyst, deposition conditions, reduction methodology, and catalytic applications. Here, a detailed discussion about the catalysts prepared by SFRD is given.

Pascu *et al.* [161] demonstrated that type of metal, metal complex, composition of supercritical reaction medium, and type of support affect the physical (PS, PSD, and morphology) and chemical properties

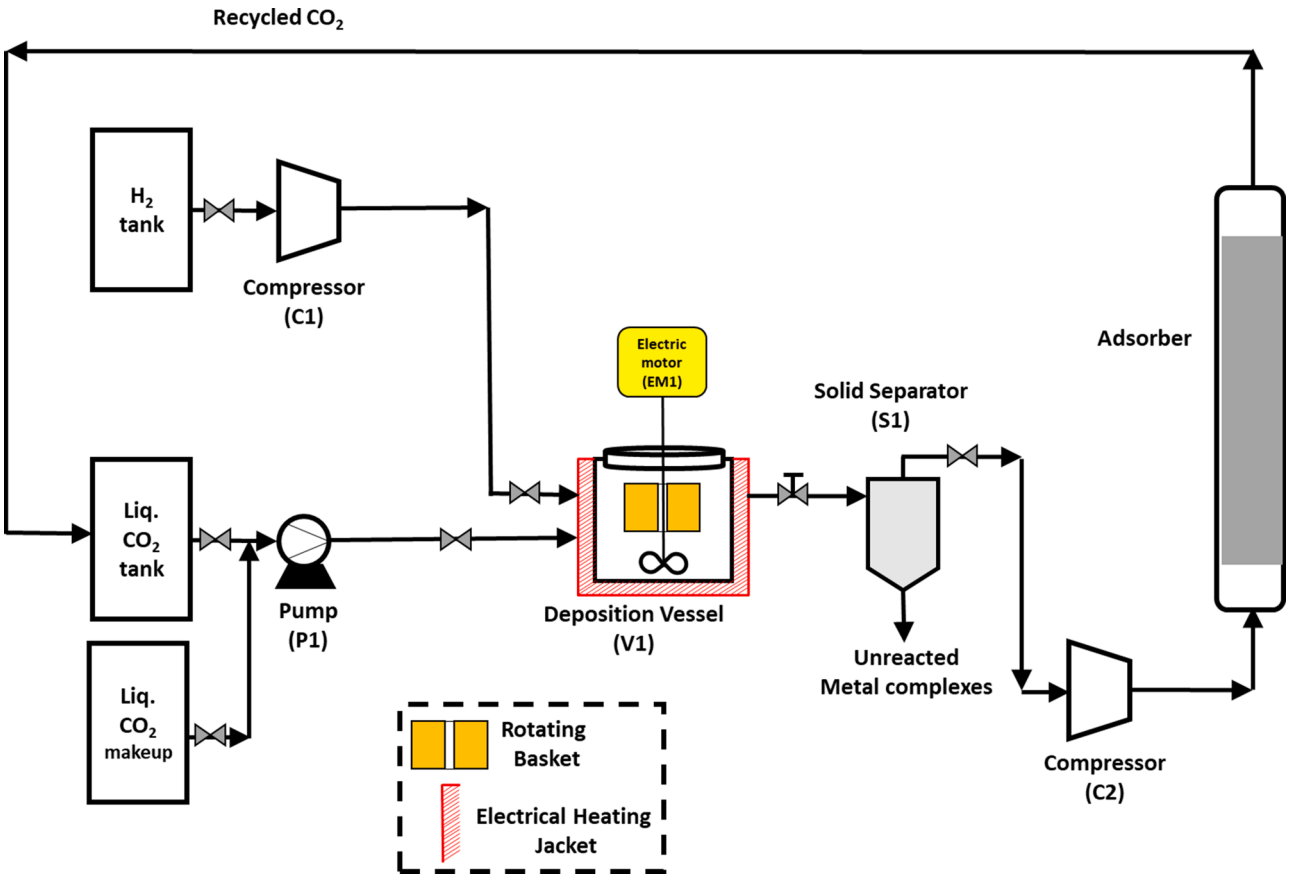

Fig. 15. Schematic process diagram of suggested large scale SFRD in a hot-wall vessel

Table 4
Summary of literature studies on catalytic applications of supported metallic NPs prepared by SFRD.

Catalyst	Temperature (°C)	Pressure (MPa)	contact time (h)	Reduction method	Reduction medium	Reduction temperature (°C)	Application	Ref.
$Pt/SnO_2/Al_2O_3$	80-100	15.5-25	20	Chemical	$scCO_2/H_2$	80-100	oxidation of carbon monoxide	[96]
Pd/SBA-15	40	8.5	3–16	Chemical	$scCO_2/H_2$ pure H_2	40	reduction of 4-nitrophenol to 4-aminophenol	[94]
$PtCuO/CeO_2/\alpha$-Al_2O_3	80	15.5	20	Chemical	$scCO_2/H_2$	80	oxidation of carbon monoxide	[162]
Ru/SBA-15	80	14	2	Chemical	$scCO_2/H_2$	150	hydrogenation of benzene and limonene	[92]
Pd/oxides Cu, Pt, Sn/SiO_2	100-200	25	1	Chemical Thermal	$scCO_2/H_2$ (chemical) $scCO_2$ (thermal)	100 (chemical) 200 (thermal)	N-alkylation of amines with alcohols	[161]
Pt/γ-Al_2O_3	80	15.5	20	chemical	$scCO_2/H_2$	80	oxidation of carbon monoxide	[97]
Pt, Ru, Ni/rGO	60-80	10-13.5	1-2	chemical	$scCO_2/H_2$ N_2/H_2	80-250 ($scCO_2/H_2$) 200-400 (N_2/H_2)	hydrogenation of limonene	[88]
PtPd/SBA-15	50	150	2	chemical	$scCO_2/H_2$	50	hydrogenation of levulinic acid (LA) to γ-valerolactone (GVL)	[98]
PtRu and PtCu/ SBA-15	60-80	13-13.5	1-4	chemical	$scCO_2/H_2$ N_2/H_2	80-200 ($scCO_2/H_2$) 200-400 (N_2/H_2)	hydrogenation of furfural	[95]
Pd/α- Al_2O_3	90	27.6	1	chemical	$scCO_2/H_2$	90	Suzuki-Miyaura Cross Coupling Reactions	[164]
Pd/MWCNT	90	27.6	1	chemical	$scCO_2/H_2$	90	Suzuki-Miyaura Cross Coupling Reactions	[165]
Pd/SBA-15	80	17.2	1	chemical	$scCO_2/H_2$	80	Suzuki-Miyaura Cross Coupling Reactions	[166]
Pt, Pd, and bimetallic PtPd /porous carbon	40-70	N/A	0.5	chemical	$scCO_2/H_2$	N/A	hydrogenation of furfural	[122]
Pt/Al_2O_3	80	15.5	20	chemical	$scCO_2/H_2$	80	oxidation of carbon monoxide and nitrogen monoxide	[163]

Table 5
Summary of literature studies on electrocatalysts prepared by SFRD.

Catalyst	Temperature (°C)	Pressure (MPa)	contact time (min)	Reduction method	Reduction medium	Reduction temperature (°C)	Application	Ref.
Pd/MWCNT	80	N/A	5-10	chemical	$H_2/scCO_2$	80	ORR	[168]
Pd/MWCNT	80	N/A	5-10	chemical	$H_2/scCO_2$	80	ORR	[169]
Pt/MWCNT	200	12	60	chemical	$H_2/scCO_2$	200	ORR	[170]
Pt/GS, Pt/CB	200	12	90	chemical	$H_2/scCO_2$	200	ORR and methanol oxidation reaction	[172]
Pd/PG, Pd/RGO, Pd/CNT, Pd/CB	50	18	300	chemical	Dimethyl amine borane	50	Formic acid and methanol oxidation reaction	[173]
Pt/Vulcan	70	24.2	24 h	physical	$scCO_2$	140	ORR	[174]
Pt/Vulcan	50	13.2	24 h	physical	$scCO_2$	120	ORR	[175]
PtRu/CNT	200	8	15	chemical	$H_2/scCO_2$	200	Methanol oxidation reaction	
PtRu/MWCT, PtCu/MWCNT, PtAu/MWCNT, PtPd/MWCNT PtNi/MWCNT	200 (70 for PtAu/ MWCNT)	10.1	60	chemical	$H_2/scCO_2$	2(70 for PtAu/ MWCNT)00	Methanol oxidation reaction	[108]
PtFe/HSG	60	30	30	chemical	Borane-THF	80	ORR	[178]
CeO_2/YSZ	NA	NA	NA	chemical	$H_2O/scCO_2$	NA	Solid oxide fuel cells	[132]
CeO_2/YSZ	60	10-15	30	chemical	$H_2O/scCO_2$	250-300	Solid oxide fuel cells	[179]
Pt/CNT	200	10	60	chemical	$H_2/scCO_2$	200	CO_2 reduction	[193]
Pd/CNT	200	10	60	chemical	$H_2/scCO_2$	200	CO_2 reduction	[194]
Cu/CNT	200	10	60	chemical	$H_2/scCO_2$	200	CO_2 reduction	[195, 196]
Au/graphene, Au/MWCNT	50	10	60	chemical	Dimethyl amine borane	50	Glucose sensor	[197]
Pd/CNT	50	10	120	Chemical	Dimethyl amine borane	50	Glucose sensor	[198]
Pd/graphene	50	10	120	Chemical	Dimethyl amine borane	50	Glucose sensor	[199]

(composition and surface chemistry) of supported metal nanocomposites prepared by SFRD. Variety of metal complexes ($Cu(hfac)_2$, $Cu(tmhd)_2$, $Pt(hfac)_2$, $Sn(hfac)_2$, and $Pd(hfac)_2$), oxide supports (SiO_2, CeO_2, Fe_2O_3, TiO_2, and ZrO_3), and different composition of reactive medium including $scCO_2$/ethanol and $scCO_2/H_2$ were used to prepare the metal nanocomposites. The catalytic performance of prepared materials was tested in N-alkylation reaction of amines with alcohols. The results showed that the physical properties of the prepared materials especially the PS of supported nanoparticles affects directly the catalytic activity and reaction yields.

Supported platinum NPs prepared by SFRD have been studied for oxidation of carbon monoxide. Garrido *et al.* [96] synthesized Pt NPs by adsorption of the metal complexe from $scCO_2$ phase on SnO_2 coated Al_2O_3 followed by reduction by adding H_2. A higher dispersion of Pt NPs (PS of 3.2 nm) and superior activity towards oxidation of carbon monoxide was observed for the catalysts prepared by SFRD compared to a catalyst prepared by wet impregnation in which the PS was 27 nm. In another study, PtCuO NPs were formed on CeO_2 coated α-Al_2O_3 sponges via simultaneous SFRD of $Cu(thd)_2$ and $Pt(cod)(me)_2$ from $scCO_2$ and reduction by adding H_2 to the supercritical medium [162]. The catalysts with different composition of active layer were tested for oxidation of carbon monoxide showing an activity two times as higher than the catalyst prepared by conventional wet impregnation method due to higher dispersion of copper species in ceria layer in the catalyst prepared by SFRD as compared to the one prepared by the conventional wet impregnation method. The higher dispersion led to an increased reducibility of Cu species as evidenced by temperature-programmed reduction (TPR) experiments, which improved catalytic activity. Comparing the TPR profiles of the catalysts showed a clear shift of reduction peaks to lower temperatures for catalyst synthesized by SRFD as compared to the reduction profile of the catalyst prepared by wet impregnation.

Recently, Casapu *et al.* [97] studied the effect of synthesis method of Pt/γ-Al_2O_3 catalysts on the PS and the PSD and their influence on the hysteresis behavior of the catalyst during oxidation of carbon monoxide. The catalysts were prepared by incipient wetness impregnation, flame spray pyrolysis, and SFRD. The lowest light-off temperature (50% conversion of CO) was observed for the catalysts prepared by SFRD with average PS of 2.1 nm and a narrow PSD. The mean PS of Pt NPs in the catalysts prepared by wet impregnation was lower than those of SFRD ones. The results showed that the combination of a narrow PSD and the presence of slightly larger Pt NPs led to a good catalytic performance which was observed in the case of catalysts prepared by SFRD. In another study performed by the same research group, it was shown that the catalysts prepared by incipient wetness impregnation exhibit fast sintering behavior due to the very small Pt PS (PS<2nm). However, the catalysts prepared by advanced methods such as SFRD and flame spray pyrolysis with slightly larger Pt NPs showed a significant deceleration of the noble metal sintering rate [163].

Morere *et al.* [92] successfully synthesized uniformly distributed Ru NPs on SBA-15 as the support using $scCO_2$. Three different approaches including deposition in $scCO_2$ followed by reduction in N_2/H_2 at atmospheric pressure, SFRD using H_2, and SFRD using ethanol were used to prepared SBA-15 supported Ru nanoparticles. In all catalysts, a homogenous particle distribution was obtained. Very small PS of Ru NPs was observed in the case of using only $scCO_2$ without H_2. However, larger Ru NPs were obtained from H_2 assisted SFRD in the form of nanorods. Using ethanol assisted SFRD led to larger Ru loading in form of nanowires. The results showed that the catalysts prepared in $scCO_2/H_2$ were more selective towards the intermediate product cyclohexene during hydrogenation of benzene compared to the commercial Ru/C catalyst. The same catalyst showed a superior activity in hydrogenation of limonene resulting in high yields of product p-menthene. In another study, they synthesized Pt, Ru, and Ni NPs on reduced graphene oxide (rGO) using SFRD in $scCO_2$ with and without adding H_2 to the supercritical medium. The size of obtained different metal NPs was in the range of 2-15 nm depending on the metal, methodology and metal loading. Pt/rGO and Ru/rGO prepared by SFRD in $scCO_2/H_2$ showed high yields and selectivities to p-menthene during partial hydrogenation of limonene [88].

Sánchez-Miguel *et al.* [95] studied the hydrogenation of furfural to furfuryl alcohol in $scCO_2$. PtRu and PtCu bimetallic NPs were deposited

on SBA-15 via both simultaneous and sequential routes followed by different chemical reductions including $scCO_2/H_2$ and N_2/H_2 in atmospheric pressure. Larger NPs were obtained via reduction in $scCO_2/H_2$ compared to the impregnation/reduction methodology. The adding of Cu and Ru to Pt led to a decrease in catalytic activity but an increase in the selectivity to furfuryl alcohol. Recently, Hu *et al.* [122] used SFRD to synthesize monometallic Pt and Pd and bimetallic PtPd NPs on a porous carbon fabricated from biomass waste sorghum. The catalysts were prepared by deposition of (Cp)Pd(allyl) and $Pt(cod)(me)_2$ from $scCO_2$ followed by reduction of the metal complexes into metallic form by adding H_2 to the supercritical medium. The materials showed significantly higher performance in terms of conversion and selectivity in hydrogenation reaction of furfural compared to the commercial ones. It was shown that the yield obtained by 3 wt% Pd/C catalysts was 7 times higher than that of commercial Pd/C with 5 wt% metal loading. The results demonstrated that using SFRD and biomass derived carbon support led to consume smaller amount of precious metals for the synthesis of the catalysts but higher catalytic performance compared to the commercial catalysts.

Qiao *et al.* [98] demonstrated that the catalytic properties of bimetallic PtPd NPs supported on SBA-15 are strongly affected by the impregnation method and type of solvents used. It was shown the catalysts prepared by SFRD exhibited high activity towards hydrogenation of levulinic acid to γ-valerolactone with a perfect selectivity compared to the ones prepared by impregnation in organic solvents such as toluene and THF. It was shown that organic solvents led to larger metallic nanoparticles as compared to the ones obtained by SFRD method, resulting in lower dispersion and conversion. Blockage of pores by agglomeration was also another reason for lower activity hindering the transport of reactants and products to and from active sites to the fluid phase. The catalyst prepared in n-pentane showed a similar activity to the one prepared by SFRD indicating that similar catalytic properties can be obtained if an organic solvent with similar properties to $scCO_2$ is chosen. In case the catalysts prepared by SFRD, it was demonstrated that Pt:Pd molar ratios in the nanoparticles affect the catalytic conversion as the catalysts with Pt:Pd ratios of 1:1 and 1:3 showed higher activity compared to the ones with ratios of 3:1, 0:1, and 1:0.

It can be concluded that preparation of supported metal NP catalysts using SFRD leads to catalysts with higher activity than the ones prepared by conventional methods such IWI and FSP. Furthermore, SFRD offers a sustainable green methodology in which one can obtain easily the desired physical and chemical properties of the nanocomposite through playing with the type of metal, type of organometallic complex, reduction methodology, type of support and condition of SCF including temperature, pressure, and the composition of the medium.

7.2. Electrocatalysis

7.2.1. Fuel Cell Applications

Fuel cells are promising devices for green and efficient electricity production. However, they have expensive components such as electrocatalysts that have high precious metal loadings, membranes for permeation of specific ion(s) and gas diffusion layers that are designed for efficient transport of reactant gases and liquid products evolved. Better and cheaper electrocatalysts are definitely needed to decrease the cost and increase the performance and SFRD technology may enable the development of such materials.

Ye *et al.*, prepared Pd NPs on MWCNT using SFRD for oxygen reduction reaction (ORR). Adsorption of palladium hexaflouroacetylacetonate hydrate ($Pd(hfa)_2.xH_2O$) metal complex on MWCNTs was carried out at 80°C and 8 MPa followed by chemical conversion by injection of H_2 [167,168]. Highly dispersed Pd NPs with 5-10 nm PS were obtained on the surface of the MWCNTs with a Pd loading of 10 wt.%. O_2 saturated cyclic voltammograms (CV) showed a cathodic current at 0.5 V (*vs.* Ag/AgCl) attributed to O_2 reduction with onset potential shifted to more positive potentials when compared to literature showing the high electrocatalytic activity of Pd/MWCNT [169]. 14 h of stability tests showed no degradation in current indicating high stability. Same group also prepared Pt/MWCNT electrocatalyst with methanol as co-solvent to dissolve $Pt(acac)_2$ in $scCO_2$ at 200°C and 8 MPa followed by injection of H_2 [170]. Uniform dispersion of Pt NPs was achieved with PS in the range of 5-10 nm at a Pt loading of 25 wt.%. Tafel slope for Pt/MWCNT was determined as -21 mV/decade which was lower than the Tafel slope of the electrocatalyst prepared by electrodeposition signifying faster kinetics [171]. Exchange current density of Pt/MWCNTs was one-order-of-magnitude higher than the commercial Pt/C electrocatalyst at a lower Pt loading indicating that SFRD resulted in highly active electrocatalysts. The electrocatalyst also showed high performance toward methanol electrooxidation.

Zhao *et al.* prepared Pt and Pd NPs on various supports for direct methanol fuel cells (DMFCs) [172,173]. $Pt(acac)_2$ was dissolved in $scCO_2$ with the aid of methanol and adsorbed on graphene sheet (GS) and Vulcan (CB) supports at 200°C and 12 MPa for 1.5 h followed by conversion with the injection of H_2 [172]. Similarly, $Pd(hfa)_2$ was dissolved in ethanol and adsorbed and simultaneously converted to Pd NPs on pristine graphene (PG), reduced graphene oxide (RGO), MWCNT and, CB supports at 50°C and 18 MPa with the addition of dimethyl amine borane (C_2H_7BN) as reducing a [173]. Dispersed Pt and Pd NPs with similar PS were obtained on GS, CB and CNT with little agglomeration caused by the addition methanol. Pd NPs on PG were highly dispersed with worm-like unique shape indicating support-solvent interaction is important for the PS and shape. Electrochemically active surface area (ESA) of Pt/GS was twice of the ESA of Pt/CB 19.2 $m^2\ g^{-1}$ due to smaller PS providing more accessible electrochemical active sites. On the other hand, Pd/PG electrocatalyst had a remarkable ESA of 115.0 m^2/g which was substantially higher than the ESA of Pd/RGO, Pd/CNT and Pd/CB. Pd/PG electrocatalyst also showed enhanced performance for methanol and formic acid oxidation perhaps due to unique shape of Pd NPs. Mass activities of both Pd- and Pt-based electrocatalysts were higher than the literature values indicating that SFRD is an effective tool for the preparation of highly active electrocatalysts.

Erkey's group investigated the preparation of electrocatalysts via SFRD with different metal complex conversion routes [174,175]. Bayrakçeken *et al.* prepared Pt/Vulcan composites using $Pt(cod)(me)_2$ as Pt metal complex by two different routes; (i) adsorption at 70 °C and 24.2 MPa followed by thermal reduction under flowing N_2 at 200 °C, and (ii) adsorption at 70 °C and 13.6 MPa followed by thermal conversion in $scCO_2$ at 140°C and 31 MPa [174]. The Pt loadings were determined as 9 wt.% for route (i) and 15 wt.% and 35 wt.% for route (ii). Conversion in $scCO_2$ is beneficial for efficient utilization of the high-priced metal complexes since all of them can be adsorbed and converted on the support while allowing one pot synthesis. Moreover, in either case homogeneously distributed Pt NPs were obtained on Vulcan with small PS (1.2, 1.3 and 2 nm for Pt loadings of 9 wt.%, 15 wt.% and 35 wt.%, respectively) indicating the effectiveness of conversion in $scCO_2$. High ESA values were obtained from the prepared electrocatalysts as 173, 125 and 87 m^2/g_{Pt}. For Pt loadings of 9 wt.%, 15 wt.% and 35 wt.%, respectively which was inversely correlated with the PS as expected. Later, Bozbag *et al.* also investigated the effect of different conversion routes on the ORR activity of Vulcan supported Pt electrocatalysts prepared via SFRD [175]. Adsorption of $Pt(cod)(me)_2$ was carried out at 50°C and 13.2 MPa followed by conversion by several different routes; (i) thermal conversion at 200°C under flowing N_2, (ii) thermal conversion in $scCO_2$ at 120°C and 26.9 MPa, and (iii) chemical conversion at 200°C under flowing H_2. Average PS increased as in the order of route(i) >route(ii)>route(iii). H_2 assisted SFRD route (ii) showed the highest electrochemical and activity values as 92.2 $m^2\ g^{-1}$ and 0.11 A mg/Pt, respectively. On the other hand, highest power density and Pt utilization were obtained for route (i) as 190 mW/cm and 380 mW/mg_{Pt}, respectively.

SFRD technique was also extended to prepare supported multimetallic NPs. The activity of bimetallic NPs depends on the metal

concentration, morphology, and atomic ordering. The technique can provide good control over these properties and exciting materials can be prepared for different applications. Lin *et al.* prepared bimetallic PtRu/CNT electrocatalysts using simultaneous SFRD for methanol electrooxidation reaction [176]. $Pt(acac)_2$ and $Ru(acac)_2$ were dissolved in $scCO_2$ with the aid of methanol and adsorbed on the CNTs at 200 °C and 8 MPa followed by reduction via H_2 injection. PtRu with PS around 5-10 nm were obtained on the surface of CNTs. Electrocatalysts showed promising activity for methanol electrooxidation which was determined through a higher I_f /I_b value and lower onset potential for methanol oxidation. PtRu/CNT also exhibited higher activity than that of the Pt/CNT (also synthesized using SFRD). Ru introduction promoted the oxidation of the strongly bound adsorbed CO on Pt as proposed in the literature [177]. Moreover, PtRu electrocatalyst was more stable than the Pt electrocatalyst. Yen *et al.*, investigated the electrochemical activities of CNT supported PtRu, PtCu, PtAu, PtPd and PtNi electrocatalysts prepared by the simultaneous SFRD for methanol electrooxidation reaction [108]. PtRu catalyst had the highest activity towards methanol oxidation over other bimetallic catalysts. Moreover, the MWCNT supported bimetallic NP catalysts all exhibited at least 60% higher I_f /I_b ratios relative to that of Pt monometallic NPs ($I_f/I_b = 1.4$). Zhou *et al.* prepared 3D honeycomb-structured graphene (HSG) supported PtFe NPs as electrocatalysts for ORR [178]. $Pt(hfa)_2$ and $Fe(acac)_2$ were dissolved in $scCO_2$ with the aid of THF and subsequently adsorbed on HSG at 60 °C and 30 MPa followed by the reduction by injection of borane-THF mixture. PtFe alloy NPs were obtained on HSG with smaller PSs (1.4-2.5 nm) than monometallic Pt/HSG (4.6 nm). After electrochemical dealloying, 14.2-fold enhancement in mass activity (1.70 A/mg_{Pt}), 11.9-fold enhancement in specific activity (1.55 mA/cm), and higher durability was obtained when compared to that of Pt/C catalyst.

Thin films have been used in wide variety of electrochemical application, however, research on thin films prepared by SFRD technique focused mainly on solid oxide fuel cell applications. Watkins and his coworkers conducted several studies on supercritical deposition of thin films for solid oxide fuel cell applications [179–181]. Bassat *et al.* deposited undoped ceria (CeO_2) films on both sides of the YSZ electrolytes as indicated in section 4 [179]. A consistent trend of decreasing polarization resistance was obtained with increasing H_2O/Ce ratio. Moreover, the polarization resistance of undoped CeO_2 films were similar to those obtained with doped CeO_2. Authors focused on optimizing the SFRD parameters of undoped CeO_2 films in their next study [180]. The effect of metal complex concentration, water content, temperature, pressure, and deposition time were explored using a cold wall reactor. Decreasing the stage temperature from 300°C to 250°C in SFRD did not significantly affect the polarization resistance. The previous findings of decrease in polarization resistance and smoother and denser films with high H_2O/Ce ratios were verified in this study as well.

7.2.2. CO_2 Electrolyzer Applications

Increasing CO_2 levels in the atmosphere caused by the continuous consumption of fossil fuels lead to global warming [182,183]. Electrochemical conversion of CO_2 to value-added carbon products is attracting a lot of interest in the last decade [184–192]. Recently there are also some efforts to extend the SFRD technology to preparation of highly active CO_2 electroreduction electrocatalysts. Rincon's group extensively investigated supported metal NPs via SFRD for CO_2 electroreduction [193–196]. Jimenez *et al.* prepared Pt, Pb and Cu supported CNT electrocatalysts via SFRD at 200°C and 10 MPa using $Pt(acac)_2$, $Pb(acac)_2$, or $Cu(acac)_2$ as metal complexes with methanol as co-solvent to dissolve the metal complexes followed by reduction by injecting H_2. Pt NPs were obtained with a bimodal PSD (3-4 nm and 8-9 nm) on the inner and outer surface of the CNTs [193]. Bimodal PSD was a result of trapped Pt NPs on the inner surface resulting in smaller PSs. As in the case of Pb, large NPs were observed with 30% of the NPs greater than 100 nm in size which was attributed to non-optimum conditions in SFRD [194]. On the other hand, Cu NPs were successfully deposited on the surface of CNTs and their sizes were in the range 2-5 nm [195,196]. Major product of Pt and Pb for CO_2 electroreduction was formic acid whereas for Cu it was CO. Moreover, methane production on Pt was favored which was determined as the second major product while on Pb electrocatalyst CO was the second major product. On Cu electrocatalyst formic acid was the second major product. Methane yields of Pb and Cu electrocatalyst was nearly the same. In all prepared electrocatalysts a small fraction of alcohols was obtained.

7.3. Sensors

Chang group extensively investigated the glucose sensing ability of different metal-carbon composites prepared via SFRD [197–199]. Wu *et al.* prepared Au/graphene and Au/CNT composites using $HAuCl_4.3H_2O$ as precursor with methanol as co-solvent at 10 MPa and 50 °C followed by reduction by introducing dimethyl amine-borane. Dispersed Au NPs were obtained on the surface of graphene and CNTs with 10 nm average PS which was significantly smaller than that reported for glucose sensor applications owing to gas-like diffusivity, low viscosity, and excellent penetration ability of $scCO_2$. When synthesis was done under air, Au NPs were significantly agglomerated. Glucose sensor electrodes were prepared with the addition of BMP-TFSI ionic liquid to improve sensing ability. Resulting electrode showed improved sensitivity for glucose detection. Furthermore, composite electrode showed good reproducibility, stability, and resistance against interfering species. Wang *et al.* prepared Pd/CNT electrodes using SFRD, in a scheme similar to that of Wu *et al.* with $Pd(hfac)_2$ as metal complex, methanol as co-solvent and dimethyl amine borane as a reducing agent [198]. PS of Pd did not change significantly by the increasing Pd loading (~5 nm). Synthesis in $scCO_2$ resulted in high dispersion of Pd NPs tightly anchored on CNT surface as evident from the TEM images.Pd/CNT electrode prepared by SFRD showed higher detection sensitivity towards glucose when compared to the one prepared via conventional deposition route. Later, Wang *et al.* prepared Pd/graphene nanocomposites with SFRD for glucose sensor applications [199]. Deposition process was the same as their previous study [198]. Highly dispersed Pd NPs were obtained on graphene surface with PSs in the range of 3-5 nm. Electrodes were modified with ionic liquid incorporation which improved the sensing performance of Pd/graphene composites. Constituent anions of the incorporated ionic liquid determined the electrochemical sensing performance.

8. Conclusion

SFRD is a promising process intensification technique for synthesis of a wide variety of nanostructured materials such as films, supported nanoparticles and metal exchanged zeolites. The enhanced mass transfer characteristics of SCFs coupled with high solubilities of reducing gases in SCFs provide many advantages related to equipment size and process time minimization over conventional techniques. The morphology and physico-chemical properties of the final material depend on a wide variety of factors such as the interaction of the metallic complex with the surface in the presence of the SCF, the reactions of the metal complexes on the surface in the presence of the SCF as well as the mass transfer processes for the metallic complexes occurring at various stages of the deposition process. Studies on the fundamental aspects of these phenomena are very rare and therefore our understanding of such phenomena is very limited. Studies on the comparison of the properties (i.e., catalytic activity and selectivity, optical properties) of the materials obtained by SFRD with the properties of the materials prepared by conventional methods are lacking and necessary for further development of this technology. With the recent developments on using SCF technology on an industrial scale for manufacturing of materials such as aerogel blankets and impregnated wood, SFRD to prepare supported metal nanostructures with its process intensification characteristics

encompassing both process miniaturization and process integration has great potential for application on an industrial scale.

Declaration of Competing Interest

The authors declare that they have no known competing financial interests or personal relationships that could have appeared to influence the work reported in this paper.

References

[1] C. Erkey, M. Türk, Chapter 4 - Fundamental aspects of pure supercritical fluids, in: E. Kiran (Ed.), Supercritical Fluid Science and Technology, Elsevier, 2021, pp. 31–49.
[2] M. Türk, Particle Formation with Supercritical Fluids: Challenges and Limitations, Elsev. Sci., 2014.
[3] J.A. Darr, M. Poliakoff, New Directions in Inorganic and Metal-Organic Coordination Chemistry in Supercritical Fluids, Chem. Rev. 99 (1999) 495–542.
[4] P.F. Siril, M. Türk, Synthesis of Metal Nanostructures Using Supercritical Carbon Dioxide: A Green and Upscalable Process, Small 16 (2020), e2001972.
[5] M. Türk, C. Erkey, Synthesis of supported nanoparticles in supercritical fluids by supercritical fluid reactive deposition: Current state, further perspectives and needs, The Journal of Supercritical Fluids 134 (2018) 176–183.
[6] V.E. Onyebuchi, A. Kolios, D.P. Hanak, C. Biliyok, V. Manovic, A systematic review of key challenges of CO2 transport via pipelines, Renewable and Sustainable Energy Reviews 81 (2018) 2563–2583.
[7] G. Brunner, Supercritical process technology related to energy and future directions – An introduction, The Journal of Supercritical Fluids 96 (2015) 11–20.
[8] O.R. Davies, A.L. Lewis, M.J. Whitaker, H. Tai, K.M. Shakesheff, S.M. Howdle, Applications of supercritical CO2 in the fabrication of polymer systems for drug delivery and tissue engineering, Adv. Drug Deliv Rev. 60 (2008) 373–387.
[9] D. Sanli, S.E. Bozbag, C. Erkey, Synthesis of nanostructured materials using supercritical CO2: Part I. Physical transformations, Journal of Materials Science 47 (2011) 2995–3025.
[10] N. Budisa, D. Schulze-Makuch, Supercritical carbon dioxide and its potential as a life-sustaining solvent in a planetary environment, Life (Basel) 4 (2014) 331–340.
[11] L. Cseri, M. Razali, P. Pogany, G. Szekely, Chapter 3.15 - Organic Solvents in Sustainable Synthesis and Engineering, in: B. Török, T. Dransfield (Eds.), Green Chemistry, Elsevier, 2018, pp. 513–553.
[12] X. Liao, H. Zhang, T. He, Preparation of Porous Biodegradable Polymer and Its Nanocomposites by Supercritical CO2Foaming for Tissue Engineering, Journal of Nanomaterials 2012 (2012) 1–12.
[13] M. Champeau, J.M. Thomassin, T. Tassaing, C. Jerome, Drug loading of polymer implants by supercritical CO2 assisted impregnation: A review, J. Control Release 209 (2015) 248–259.
[14] H.A. Eren, O. Avinc, S. Eren, Supercritical carbon dioxide for textile applications and recent developments, IOP Conference Series: Materials Science and Engineering (2017) 254.
[15] D. Gao, D.-f. Yang, H.-s. Cui, T.-t. Huang, J.-x. Lin, Supercritical Carbon Dioxide Dyeing for PET and Cotton Fabric with Synthesized Dyes by a Modified Apparatus, ACS Sustainable Chemistry & Engineering 3 (2015) 668–674.
[16] R.F.H. Hernandha, P.C. Rath, B. Umesh, J. Patra, C.Y. Huang, W.W. Wu, Q. F. Dong, J. Li, J.K. Chang, Supercritical CO2-Assisted SiOx/Carbon Multi-Layer Coating on Si Anode for Lithium-Ion Batteries, Advanced Functional Materials 31 (2021).
[17] F.H.M. van Zelst, S.G.J. van Meerten, P.J.M. van Bentum, A.P.M. Kentgens, Hyphenation of Supercritical Fluid Chromatography and NMR with In-Line Sample Concentration, Anal. Chem. 90 (2018) 10457–10464.
[18] G.L. Weibel, C.K. Ober, An overview of supercritical CO2 applications in microelectronics processing, Microelectronic Engineering 65 (2003) 145–152.
[19] O. Parenago, A. Rybaltovsky, E. Epifanov, A. Shubnyi, G. Bragina, A. Lazhko, D. Khmelenin, V. Yusupov, N. Minaev, Synthesis of Supported Heterogeneous Catalysts by Laser Ablation of Metallic Palladium in Supercritical Carbon Dioxide Medium, Molecules 25 (2020).
[20] H. Grajek, Regeneration of Adsorbents by the Use of Liquid, Subcritical and Supercritical Carbon Dioxide, Adsorption Science & Technology 18 (2000) 347–371.
[21] C. Burda, X. Chen, R. Narayanan, M.A. El-Sayed, Chemistry and properties of nanocrystals of different shapes, Chem. Rev. 105 (2005) 1025–1102.
[22] C. Erkey, Supercritical Fluids and Organometallic Compounds: From Recovery of Trace Metals to Synthesis of Nanostructured Materials, Elsevier Science, 2011.
[23] C. Erkey, Preparation of metallic supported nanoparticles and films using supercritical fluid deposition, The Journal of Supercritical Fluids 47 (2009) 517–522.
[24] S.E. Bozbag, D. Sanli, C. Erkey, Synthesis of nanostructured materials using supercritical CO2: Part II. Chemical transformations, Journal of Materials Science 47 (2011) 3469–3492.
[25] S.E. Bozbağ, C. Erkey, Supercritical deposition: Current status and perspectives for the preparation of supported metal nanostructures, The Journal of Supercritical Fluids 96 (2015) 298–312.
[26] S.B. Barim, E. Uzunlar, S.E. Bozbag, C. Erkey, Supercritical Deposition: A Powerful Technique for Synthesis of Functional Materials for Electrochemical Energy Conversion and Storage, Journal of The Electrochemical Society 167 (2020).
[27] M. Majimel, S. Marre, E. Garrido, C. Aymonier, Supercritical Fluid Chemical Deposition as an Alternative Process to CVD for the Surface Modification of Materials, Chemical Vapor Deposition 17 (2011) 342–352.
[28] K.J. Hüttinger, CVD in Hot Wall Reactors—The Interaction Between Homogeneous Gas-Phase and Heterogeneous Surface Reactions, 4 (1998) 151-158.
[29] C. Erkey, M. Türk, Chapter 7 - Synthesis of nanostructured composites of metals by supercritical deposition (SCD), in: E. Kiran (Ed.), Supercritical Fluid Science and Technology, Elsevier, 2021, pp. 129–209.
[30] W.H. Teoh, R. Mammucari, N.R. Foster, Solubility of organometallic complexes in supercritical carbon dioxide: A review, Journal of Organometallic Chemistry 724 (2013) 102–116.
[31] O. Aschenbrenner, S. Kemper, N. Dahmen, K. Schaber, E. Dinjus, Solubility of β-diketonates, cyclopentadienyls, and cyclooctadiene complexes with various metals in supercritical carbon dioxide, The Journal of Supercritical Fluids 41 (2007) 179–186.
[32] C. Erkey, Supercritical carbon dioxide extraction of metals from aqueous solutions: a review, The Journal of Supercritical Fluids 17 (2000) 259–287.
[33] N. Smart, Solubility of chelating agents and metal-containing compounds in supercritical fluid carbon dioxide, Talanta 44 (1997) 137–150.
[34] Ž. Knez, D. Cör, M.Knez Hrnčič, Solubility of Solids in Sub- and Supercritical Fluids: A Review 2010–2017, Journal of Chemical & Engineering Data 63 (2017) 860–884.
[35] S.G. Kazarian, M.F. Vincent, F.V. Bright, C.L. Liotta, C.A. Eckert, Specific Intermolecular Interaction of Carbon Dioxide with Polymers, Journal of the American Chemical Society 118 (1996) 1729–1736.
[36] M. Haruki, F. Kobayashi, S.-i. Kihara, S. Takishima, Solubility of β-Diketonate Complexes of Copper(II) and Cobalt(II) in Supercritical Carbon Dioxide, Journal of Chemical & Engineering Data 56 (2011) 2230–2235.
[37] A.F. Lagalante, B.N. Hansen, T.J. Bruno, R.E. Sievers, Solubilities of Copper(II) and Chromium(III) .beta.-Diketonates in Supercritical Carbon Dioxide, Inorganic Chemistry 34 (2002) 5781–5785.
[38] M. Ashraf-Khorassani, M.T. Combs, L.T. Taylor, Solubility of metal chelates and their extraction from an aqueous environment via supercritical CO2, Talanta 44 (1997) 755–763.
[39] M.Z. Özel, K.D. Bartle, A.A. Clifford, M.D. Burford, Extraction, solubility and stability of metal complexes using stainless steel supercritical fluid extraction system, Analytica Chimica Acta 417 (2000) 177–184.
[40] R.B. Gupta, J.-J. Shim, Solubility in supercritical carbon dioxide, CRC press, 2006.
[41] L. Fu, Z.M. Liu, Y.Q. Liu, B.X. Han, J.Q. Wang, P.A. Hu, L.C. Cao, D.B. Zhu, Coating Carbon Nanotubes with Rare Earth Oxide Multiwalled Nanotubes, Advanced Materials 16 (2004) 350–352.
[42] L. Fu, Y.Q. Liu, Z.M. Liu, B.X. Han, L.C. Cao, D.C. Wei, G. Yu, D.B. Zhu, Carbon Nanotubes Coated with Alumina as Gate Dielectrics of Field-Effect Transistors, Advanced Materials 18 (2006) 181–185.
[43] L. Fu, Z. Liu, Y. Liu, B. Han, P. Hu, L. Cao, D. Zhu, Beaded Cobalt Oxide Nanoparticles along Carbon Nanotubes: Towards More Highly Integrated Electronic Devices, Advanced Materials 17 (2005) 217–221.
[44] Z. Sun, H. Yuan, Z. Liu, B. Han, X. Zhang, A Highly Efficient Chemical Sensor Material for H2S: α-Fe2O3 Nanotubes Fabricated Using Carbon Nanotube Templates, Advanced Materials 17 (2005) 2993–2997.
[45] Z. Sun, X. Zhang, N. Na, Z. Liu, B. Han, G. An, Synthesis of ZrO2-carbon nanotube composites and their application as chemiluminescent sensor material for ethanol, J. Phys. Chem. B. 110 (2006) 13410–13414.
[46] Z. Sun, X. Zhang, B. Han, Y. Wu, G. An, Z. Liu, S. Miao, Z. Miao, Coating carbon nanotubes with metal oxides in a supercritical carbon dioxide–ethanol solution, Carbon 45 (2007) 2589–2596.
[47] G. An, P. Yu, M. Xiao, Z. Liu, Z. Miao, K. Ding, L. Mao, Low-temperature synthesis of Mn(3)O(4) nanoparticles loaded on multi-walled carbon nanotubes and their application in electrochemical capacitors, Nanotechnology 19 (2008), 275709.
[48] G. An, Y. Zhang, Z. Liu, Z. Miao, B. Han, S. Miao, J. Li, Preparation of porous chromium oxide nanotubes using carbon nanotubes as templates and their application as an ethanol sensor, Nanotechnology 19 (2008), 035504.
[49] Z. Sun, Z. Liu, B. Han, G. An, Supercritical carbon dioxide-assisted deposition of tin oxide on carbon nanotubes, Materials Letters 61 (2007) 4565–4568.
[50] M.J. Tenorio, S. Ginés, C. Pando, J.A.R. Renuncio, A. Cabañas, Solubility of the Metal Precursor Ni(NO3)2•6H2O in High-Pressure CO2 + Ethanol Mixtures, Journal of Chemical & Engineering Data 63 (2017) 1065–1071.
[51] J. Ming, C. Wu, H. Cheng, Y. Yu, F. Zhao, Reaction of hydrous inorganic metal salts in CO2 expanded ethanol: Fabrication of nanostructured materials via supercritical technology, The Journal of Supercritical Fluids 57 (2011) 137–142.
[52] W. Cross, A. Akgerman, C. Erkey, Determination of metal-chelate complex solubilities in supercritical carbon dioxide, Industrial & engineering chemistry research 35 (1996) 1765–1770.
[53] N.G. Smart, T. Carleson, T. Kast, A.A. Clifford, M.D. Burford, C.M. Wai, Solubility of chelating agents and metal-containing compounds in supercritical fluid carbon dioxide, Talanta 44 (1997) 137–150.
[54] W.C. Andersen, R.E. Sievers, A.F. Lagalante, T.J. Bruno, Solubilities of cerium (IV), terbium (III), and iron (III) β-diketonates in supercritical carbon dioxide, Journal of Chemical & Engineering Data 46 (2001) 1045–1049.
[55] I. Ushiki, R. Fujimitsu, S. Takishima, Predicting the solubilities of metal acetylacetonates in supercritical CO2: Thermodynamic approach using PC-SAFT, The Journal of Supercritical Fluids 164 (2020).

[56] P.F. Siril, M. Türk, Synthesis of Metal Nanostructures Using Supercritical Carbon Dioxide: A Green and Upscalable Process, Small 16 (2020), 2001972.
[57] M.J. Tenorio, C. Pando, J.A.R. Renuncio, J.G. Stevens, R.A. Bourne, M. Poliakoff, A. Cabañas, Adsorption of Pd(hfac)2 on mesoporous silica SBA-15 using supercritical CO2 and its role in the performance of Pd–SiO2 catalyst, The Journal of Supercritical Fluids 69 (2012) 21–28.
[58] C.D. Saquing, T.T. Cheng, M. Aindow, C. Erkey, Preparation of platinum/carbon aerogel nanocomposites using a supercritical deposition method, Journal of Physical Chemistry B 108 (2004) 7716–7722.
[59] I. Ushiki, M. Koike, T. Shimizu, Y. Sato, S. Takishima, H. Inomata, Measurement and modeling of adsorption equilibria of cobalt (III) acetylacetonate on MCM-41 mesoporous silica in the presence of supercritical carbon dioxide with methanol co-solvent, The Journal of Supercritical Fluids 140 (2018) 329–335.
[60] I. Ushiki, N. Takahashi, T. Shimizu, Y. Sato, M. Ota, R.L. Smith, H. Inomata, Adsorption equilibria of rhodium acetylacetonate with MCM-41, MSU-H, and HMS silica substrates in supercritical carbon dioxide for preparing catalytic mesoporous materials, The Journal of Supercritical Fluids 120 (2017) 240–248.
[61] M.M. Dubinin, V.A. Astakhov, Description of Adsorption Equilibria of Vapors on Zeolites over Wide Ranges of Temperature and Pressure. Molecular Sieve Zeolites-II, AMERICAN CHEMICAL SOCIETY, 1971, pp. 69–85.
[62] R. Humayun, D.L. Tomasko, High-resolution adsorption isotherms of supercritical carbon dioxide on activated carbon, AIChE Journal 46 (2000) 2065–2075.
[63] S.E. Bozbag, L.C. Zhang, M. Aindow, C. Erkey, Carbon aerogel supported nickel nanoparticles and nanorods using supercritical deposition, The Journal of Supercritical Fluids 66 (2012) 265–273.
[64] S.E. Bozbag, S.O. Kostenko, M.A. Kurykin, V.N. Khrustalev, A.R. Khokhlov, L. Zhang, M. Aindow, C. Erkey, Aerogel-Copper Nanocomposites Prepared Using the Adsorption of a Polyfluorinated Complex from Supercritical CO2, Journal of Nanoparticle Research 14 (2012) 973–986.
[65] C. Erkey, Supercritical Fluids & Organometallic Compounds, Elsevier, Amsterdam, 2011.
[66] C.S. Tan, D.C. Liou, Adsorption Equilibrium of Toluene From Supercritical Carbon-Dioxide on Actıvated Carbon, Industrial & Engineering Chemistry Research 29 (1990) 1412–1415.
[67] G. Afrane, E.H. Chimowitz, A molecular thermodynamic model for adsorption equilibrium from supercritical fluids, The Journal of Supercritical Fluids 6 (1993) 143–154.
[68] F.D. Kelley, E.H. Chimowitz, NEAR-CRITICAL PHENOMENA AND RESOLUTION IN SUPERCRITICAL FLUID CHROMATOGRAPHY, Aiche Journal 36 (1990) 1163–1175.
[69] Q.-q. Xu, Y.-q. Wang, A.-q. Wang, J.-z. Yin, Systematical study of depositing nanoparticles and nanowires in mesoporous silica using supercritical carbon dioxide and co-solvents: morphology control, thermodynamics and kinetics of adsorption, Nanotechnology 23 (2012), 285602.
[70] C. Erkey, Chapter 4 - Thermodynamics and Dynamics of Adsorption of Metal Complexes on Surfaces from Supercritical Solutions, in: C. Erkey (Ed.), Supercritical Fluid Science and Technology, Elsevier, 2011, pp. 41–77.
[71] M. Toriumi, R. Katooka, K. Yui, T. Funazukuri, C.Y. Kong, S. Kagei, Measurements of binary diffusion coefficients for metal complexes in organic solvents by the Taylor dispersion method, Fluid Phase Equilibria 297 (2010) 62–66.
[72] C.Y. Kong, Y.Y. Gu, M. Nakamura, T. Funazukuri, S. Kagei, Diffusion coefficients of metal acetylacetonates in supercritical carbon dioxide, Fluid Phase Equilibria 297 (2010) 162–167.
[73] C. Erkey, M. Türk, Chapter 5 - Thermodynamics and transport properties of mixtures composed of metal complexes and supercritical fluids, in: E. Kiran (Ed.), Supercritical Fluid Science and Technology, Elsevier, 2021, pp. 51–71.
[74] Y. Zhang, B. Cangul, Y. Garrabos, C. Erkey, Thermodynamics and kinetics of adsorption of bis(2,2,6,6-tetramethyl-3,5-heptanedionato) (1,5-cyclooctadiene) ruthenium (II) on carbon aerogel from supercritical CO2 solution, The Journal of Supercritical Fluids 44 (2008) 71–77.
[75] B. Cangül, L.C. Zhang, M. Aindow, C. Erkey, Preparation of carbon black supported Pd, Pt and Pd–Pt nanoparticles using supercritical CO2 deposition, The Journal of Supercritical Fluids 50 (2009) 82–90.
[76] S.E. Bozbag,, N.S. Yasar,, L.C. Zhang,, M. Aindow,, C. Erkey,, Adsorption of Pt (cod)me2 onto organic aerogels from supercritical solutions for the synthesis of supported platinum nanoparticles, 56 (2011) 105-113.
[77] I. Ushiki, N. Takahashi, M. Koike, Y. Sato, S. Takishima, H. Inomata, Adsorption kinetics of rhodium (III) acetylacetonate onto mesoporous silica adsorbents in the presence of supercritical carbon dioxide, The Journal of Supercritical Fluids 135 (2018) 137–144.
[78] S. Brunauer, P.H. Emmett, E. Teller, Adsorption of Gases in Multimolecular Layers, Journal of the American Chemical Society 60 (1938) 309–319.
[79] E.P. Barrett, L.G. Joyner, P.P. Halenda, The Determination of Pore Volume and Area Distributions in Porous Substances. I. Computations from Nitrogen Isotherms, Journal of the American Chemical Society 73 (1951) 373–380.
[80] T. Funazukuri, C.Y. Kong, S. Kagei, Impulse response techniques to measure binary diffusion coefficients under supercritical conditions, Journal of Chromatography A 1037 (2004) 411–429.
[81] O. Aschenbrenner, N. Dahmen, K. Schaber, E. Dinjus, Adsorption of Dimethyl(1,5-cyclooctadiene)platinum on Porous Supports in Supercritical Carbon Dioxide, Industrial & Engineering Chemistry Research 47 (2008) 3150–3155.
[82] J. Baek, B. Rungtaweevoranit, X. Pei, M. Park, S.C. Fakra, Y.S. Liu, R. Matheu, S. A. Alshmimri, S. Alshehri, C.A. Trickett, G.A. Somorjai, O.M. Yaghi, Bioinspired Metal-Organic Framework Catalysts for Selective Methane Oxidation to Methanol, J. Am. Chem. Soc. 140 (2018) 18208–18216.
[83] H. Liu, E.A. Macedo, Accurate correlations for the self-diffusion coefficients of CO2, CH4, C2H4, H2O, and D2O over wide ranges of temperature and pressure, The Journal of Supercritical Fluids 8 (1995) 310–317.
[84] S.E. Bozbag, U. Unal, M.A. Kurykin, C.J. Ayala, M. Aindow, C. Erkey, Thermodynamic Control of Metal Loading and Composition of Carbon Aerogel Supported Pt–Cu Alloy Nanoparticles by Supercritical Deposition, The Journal of Physical Chemistry C 117 (2013) 6777–6787.
[85] Á. Sastre,, Á. Martín, E. Alonso, Adsorption of nickelocene and ruthenocene on mesoporous silica MCM-48 and activated carbon supports in supercritical carbon dioxide, 117 (2016) 138-146.
[86] W.J. Weber, J.C. Morris, Kinetics of Adsorption on Carbon from Solution, Journal of the Sanitary Engineering Division 89 (1963) 31–59.
[87] X.R. Ye, Y. Lin, C.M. Wai, Decorating catalytic palladium nanoparticles on carbon nanotubes in supercritical carbon dioxide, Chem. Commun. (Camb.) (2003) 642–643.
[88] J. Morère, E. Sánchez-Miguel, M.J. Tenorio, C. Pando, A. Cabañas, Supercritical fluid preparation of Pt, Ru and Ni/graphene nanocomposites and their application as selective catalysts in the partial hydrogenation of limonene, The Journal of Supercritical Fluids 120 (2017) 7–17.
[89] J.J. Watkins, T.J. McCarthy, Polymer/Metal Nanocomposite Synthesis in Supercritical CO2, Chemistry of Materials 7 (2002) 1991–1994.
[90] C.D. Saquing, D. Kang, M. Aindow, C. Erkey, Investigation of the supercritical deposition of platinum nanoparticles into carbon aerogels, Microporous and Mesoporous Materials 80 (2005) 11–23.
[91] S. Marre, A. Erriguible, A. Perdomo, F. Cansell, F. Marias, C. Aymonier, Kinetically Controlled Formation of Supported Nanoparticles in Low Temperature Supercritical Media for the Development of Advanced Nanostructured Materials, The Journal of Physical Chemistry C 113 (2009) 5096–5104.
[92] J. Morère, M.J. Torralvo, C. Pando, J.A.R. Renuncio, A. Cabañas, Supercritical fluid deposition of Ru nanoparticles onto SiO2 SBA-15 as a sustainable method to prepare selective hydrogenation catalysts, RSC Advances 5 (2015) 38880–38891.
[93] X.-R. Ye, Y. Lin, C. Wang, M.H. Engelhard, Y. Wang, C.M. Wai, Supercritical fluid synthesis and characterization of catalytic metal nanoparticles on carbon nanotubes, Journal of Materials Chemistry 14 (2004).
[94] J. Morère, M.J. Tenorio, M.J. Torralvo, C. Pando, J.A.R. Renuncio, A. Cabañas, Deposition of Pd into mesoporous silica SBA-15 using supercritical carbon dioxide, The Journal of Supercritical Fluids 56 (2011) 213–222.
[95] E. Sánchez-Miguel, M.J. Tenorio, J. Morère, A. Cabañas, Green preparation of PtRu and PtCu/SBA-15 catalysts using supercritical CO 2, Journal of CO2 Utilization 22 (2017) 382–391.
[96] G.I. Garrido, F.C. Patcas, G. Upper, M. Türk, S. Yilmaz, B. Kraushaar-Czarnetzki, Supercritical deposition of Pt on SnO2-coated Al2O3 foams: Phase behaviour and catalytic performance, Applied Catalysis A: General 338 (2008) 58–65.
[97] M. Casapu, A. Fischer, A.M. Gänzler, R. Popescu, M. Crone, D. Gerthsen, M. Türk, J.-D. Grunwaldt, Origin of the Normal and Inverse Hysteresis Behavior during CO Oxidation over Pt/Al2O3, ACS Catalysis 7 (2016) 343–355.
[98] Y. Qiao, N. Said, M. Rauser, K. Yan, F. Qin, N. Theyssen, W. Leitner, Preparation of SBA-15 supported Pt/Pd bimetallic catalysts using supercritical fluid reactive deposition: how do solvent effects during material synthesis affect catalytic properties? Green Chemistry 19 (2017) 977–986.
[99] S. Wolff, M. Crone, T. Müller, M. Enders, S. Bräse, M. Türk, Preparation of supported Pt nanoparticles by supercritical fluid reactive deposition: Influence of precursor, substrate and pressure on product properties, The Journal of Supercritical Fluids 95 (2014) 588–596.
[100] V. Aggarwal, L.F. Reichenbach, M. Enders, T. Müller, S. Wolff, M. Crone, M. Türk, S. Bräse, Influence of perfluorinated end groups on the SFRD of [Pt(cod)Me(C(n)F (2n+1))] onto porous Al(2)O(3) in CO(2) under reductive conditions, Chemistry 19 (2013) 12794–12799.
[101] S.B. Barim, S.E. Bozbag, B. Deljoo, M. Aindow, C. Erkey, Highly Active Carbon Supported PtCu Electrocatalysts for PEMFCs by in situ Supercritical Deposition Coupled with Electrochemical Dealloying, Fuel Cells 20 (2019) 285–299.
[102] S. Müller, M. Türk, Production of supported gold and gold–silver nanoparticles by supercritical fluid reactive deposition: Effect of substrate properties, The Journal of Supercritical Fluids 96 (2015) 287–297.
[103] S.G. Aspromonte, Á. Sastre, A.V. Boix, M.J. Cocero, E. Alonso, Cobalt oxide nanoparticles on mesoporous MCM-41 and Al-MCM-41 by supercritical CO2 deposition, Microporous and Mesoporous Materials 148 (2012) 53–61.
[104] H. Gunes, Y. Özbakir, S.B. Barim, H. Yousefzadeh, S.E. Bozbag, C. Erkey, A Remarkable Class of Nanocomposites: Aerogel Supported Bimetallic Nanoparticles, Frontiers in Materials 7 (2020).
[105] J.E. Mondloch, E. Bayram, R.G. Finke, A review of the kinetics and mechanisms of formation of supported-nanoparticle heterogeneous catalysts, Journal of Molecular Catalysis A: Chemical 355 (2012) 1–38.
[106] R. Ferrando, J. Jellinek, R.L. Johnston, Nanoalloys: from theory to applications of alloy clusters and nanoparticles, Chem. Rev. 108 (2008) 845–910.
[107] Y. Lin, X. Cui, C.H. Yen, C.M. Wai, PtRu/carbon nanotube nanocomposite synthesized in supercritical fluid: a novel electrocatalyst for direct methanol fuel cells, Langmuir 21 (2005) 11474–11479.
[108] C.H. Yen, K. Shimizu, Y.-Y. Lin, F. Bailey, I.F. Cheng, C.M. Wai, Chemical Fluid Deposition of Pt-Based Bimetallic Nanoparticles on Multiwalled Carbon Nanotubes for Direct Methanol Fuel Cell Application, Energy & Fuels 21 (2007) 2268–2271.
[109] G. Qiao, Q. Xu, A. Wang, D. Zhou, J. Yin, Desorption-dominated synthesis of CuO/SBA-15 with tunable particle size and loading in supercritical CO2, Nanotechnology 31 (2019), 095602.

[110] G.-Y. Qiao, Q.-Q. Xu, A. Wang, J.-T. Liu, D. Zhou, Z. Duan, J.-Z. Yin, Size-controlled synthesis of CuO nanoparticles by the supercritical antisolvent method in SBA-15, ACS Sustainable Chemistry & Engineering 9 (2020) 129–136.
[111] G. Qiao, Q. Xu, A. Wang, D. Zhou, J. Yin, Efficient synthesis of sub-5 nm Ag nanoparticles by the desorption effect of supercritical CO2 in SBA-15, Nanotechnology 31 (2020), 375603.
[112] Y. Zhao, J. Zhang, J. Song, J. Li, J. Liu, T. Wu, P. Zhang, B. Han, Ru nanoparticles immobilized on metal–organic framework nanorods by supercritical CO 2-methanol solution: highly efficient catalyst, Green Chemistry 13 (2011) 2078–2082.
[113] H. Yousefzadeh, S.E. Bozbag, C. Erkey, Supercritical ion exchange: A new method to synthesize copper exchanged zeolites, The Journal of Supercritical Fluids 179 (2022).
[114] Y. Zong, J.J. Watkins, Deposition of Copper by the H2-Assisted Reduction of Cu (tmod)2 in Supercritical Carbon Dioxide: Kinetics and Reaction Mechanism, Chemistry of Materials 17 (2005) 560–565.
[115] J.M. Blackburn, D.P. Long, A. Cabanas, J.J. Watkins, Deposition of conformal copper and nickel films from supercritical carbon dioxide, Science 294 (2001) 141–145.
[116] A. Cabañas, D.P. Long, J.J. Watkins, Deposition of Gold Films and Nanostructures from Supercritical Carbon Dioxide, Chemistry of Materials 16 (2004) 2028–2033.
[117] B. Giroire, M.A. Ahmad, G. Aubert, L. Teulé-Gay, D. Michau, J.J. Watkins, C. Aymonier, A. Poulon-Quintin, A comparative study of copper thin films deposited using magnetron sputtering and supercritical fluid deposition techniques, Thin Solid Films 643 (2017) 53–59.
[118] Y. Zhang, C. Erkey, Preparation of supported metallic nanoparticles using supercritical fluids: A review, The Journal of Supercritical Fluids 38 (2006) 252–267.
[119] A.H. Romang, J.J. Watkins, Supercritical fluids for the fabrication of semiconductor devices: emerging or missed opportunities? Chem. Rev. 110 (2010) 459–478.
[120] S.E. Bozbag, C. Erkey, Supercritical fluids in fuel cell research and development, The Journal of Supercritical Fluids 62 (2012) 1–31.
[121] P.G. Corradini, F.I. Pires, V.A. Paganin, J. Perez, E. Antolini, Effect of the relationship between particle size, inter-particle distance, and metal loading of carbon supported fuel cell catalysts on their catalytic activity, Journal of Nanoparticle Research 14 (2012).
[122] D. Hu, H. Xu, Z. Yi, Z. Chen, C. Ye, Z. Wu, H.F. Garces, K. Yan, Green CO2-Assisted Synthesis of Mono- and Bimetallic Pd/Pt Nanoparticles on Porous Carbon Fabricated from Sorghum for Highly Selective Hydrogenation of Furfural, ACS Sustainable Chemistry & Engineering 7 (2019) 15339–15345.
[123] S.B. Barim, S.E. Bozbag, H. Yu, R. Kızılel, M. Aindow, C. Erkey, Mesoporous carbon aerogel supported PtCu bimetallic nanoparticles via supercritical deposition and their dealloying and electrocatalytic behaviour, Catalysis Today 310 (2018) 166–175.
[124] K.S. Morley, P. Licence, P.C. Marr, J.R. Hyde, P.D. Brown, R. Mokaya, Y. Xia, S. M. Howdle, Supercritical fluids: A route to palladium-aerogel nanocomposites, Journal of Materials Chemistry 14 (2004).
[125] B. Giroire, M.Ali Ahmad, G. Aubert, L. Teule-Gay, D. Michau, J.J. Watkins, C. Aymonier, A. Poulon-Quintin, A comparative study of copper thin films deposited using magnetron sputtering and supercritical fluid deposition techniques, Thin Solid Films 643 (2017) 53–59.
[126] E.T. Hunde, J.J. Watkins, Reactive deposition of cobalt and nickel films from their metallocenes in supercritical carbon dioxide solution, Chemistry of Materials 16 (2004) 498–503.
[127] N.E. Fernandes, S.M. Fisher, J.C. Poshusta, D.G. Vlachos, M. Tsapatsis, J. J. Watkins, Reactive Deposition of Metal Thin Films within Porous Supports from Supercritical Fluids, Chemistry of Materials 13 (2001) 2023–2031.
[128] X. Shan, D.P. Schmidt, J.J. Watkins, Study of natural convection in supercritical CO2 cold wall reactors: Simulations and experiments, The Journal of Supercritical Fluids 40 (2007) 84–92.
[129] A. O'Nei, J.J. Watkins, Reactive Deposition of Conformal Metal Oxide Films from Supercritical Carbon Dioxide, Chemistry of Materials 19 (2007) 5460–5466.
[130] D. Mesguich, C. Aymonier, J.-M. Bassat, F. Mauvy, E. You, J.J. Watkins, Low-Temperature Deposition of Undoped Ceria Thin Films in scCO2 As Improved Interlayers for IT-SOFC, Chemistry of Materials 23 (2011) 5323–5330.
[131] A. Cabanas, D.P. Long, J.J. Watkins, Deposition of gold films and nanostructures from supercritical carbon dioxide, Chemistry of Materials 16 (2004) 2028–2033.
[132] J.-M. Bassat, D. Mesguich, C. Ferchaud, Y. Zhang-Steenwinkel, F. Van Berkel, C. Aymonier, J. Watkins, J.-C. Grenier, Doped/Undoped Ceria Buffer Layers for Improved LT SOFC Performances with Pr2NiO4+ δ Cathode, ECS Transactions 35 (2011) 1945.
[133] Y. Zhao, K. Jung, Y. Shimoyama, Y. Shimogaki, T. Momose, Conformal bismuth titanate formation using supercritical fluid deposition, ECS Journal of Solid State Science and Technology 6 (2017) P483.
[134] E. Kondoh, Synthesis and Characterization of Ni-Pt Alloy Thin Films Prepared by Supercritical Fluid Chemical Deposition Technique, Nanomaterials 11 (2021) 151.
[135] Q.Le Trequesser, D. Mesguich, E. You, C. Aymonier, J.J. Watkins, Supercritical fluid deposition of compositionally uniform yttria stabilized zirconia films, The Journal of Supercritical Fluids 66 (2012) 328–332.
[136] J.A. Branch, P.N. Bartlett, Electrochemistry in supercritical fluids, Philosophical Transactions of the Royal Society a-Mathematical Physical and Engineering Sciences (2015) 373.
[137] P.N. Bartlett, D.A. Cook, M.W. George, A.L. Hector, J. Ke, W. Levason, G. Reid, D. C. Smith, W. Zhang, Electrodeposition from supercritical fluids, Physical Chemistry Chemical Physics 16 (2014) 9202–9219.
[138] A.C. McDonald, F.R.F. Fan, A.J. Bard, Electrochemistry in near-critical and supercritical fluids. 2. Water. Experimental techniques and the copper(II) system, The Journal of Physical Chemistry 90 (1986) 196–202.
[139] J. Ke, W.T. Su, S.M. Howdle, M.W. George, D. Cook, M. Perdjon-Abel, P. N. Bartlett, W.J. Zhang, F. Cheng, W. Levason, G. Reid, J. Hyde, J. Wilson, D. C. Smith, K. Mallik, P. Sazio, Electrodeposition of metals from supercritical fluids, Proceedings of the National Academy of Sciences of the United States of America 106 (2009) 14768–14772.
[140] J. Ke, P.N. Bartlett, D. Cook, T.L. Easun, M.W. George, W. Levason, G. Reid, D. Smith, W.T. Su, W.J. Zhang, Electrodeposition of germanium from supercritical fluids, Physical Chemistry Chemical Physics 14 (2012) 1517–1528.
[141] P.N. Bartlett, M. Perdjon-Abel, D. Cook, G. Reid, W. Levason, F. Cheng, W. J. Zhang, M.W. George, J. Ke, R. Beanland, J. Sloan, The Electrodeposition of Silver from Supercritical Carbon Dioxide/Acetonitrile, Chemelectrochem 1 (2014) 187–194.
[142] P.N. Bartlett, J. Burt, D.A. Cook, C.Y. Cummings, M.W. George, A.L. Hector, M. M. Hasan, J. Ke, W. Levason, D. Pugh, G. Reid, P.W. Richardson, D.C. Smith, J. Spencer, N. Suleiman, W.J. Zhang, A Versatile Precursor System for Supercritical Fluid Electrodeposition of Main-Group Materials, Chemistry-a European Journal 22 (2016) 302–309.
[143] P.N. Bartlett, D.A. Cook, M.M. Hasan, A.L. Hector, S. Marks, J. Naik, G. Reid, J. Sloan, D.C. Smith, J. Spencer, Z. Webber, Supercritical fluid electrodeposition, structural and electrical characterisation of tellurium nanowires, Rsc Advances 7 (2017) 40720–40726.
[144] P.N. Bartlett, R. Beanland, J. Burt, M.M. Hasan, A.L. Hector, R.J. Kashtiban, W. Levason, A.W. Lodge, S. Marks, J. Naik, A. Rind, G. Reid, P.W. Richardson, J. Sloan, D.C. Smith, Exploration of the Smallest Diameter Tin Nanowires Achievable with Electrodeposition: Sub 7 nm Sn Nanowires Produced by Electrodeposition from a Supercritical Fluid, Nano Letters 18 (2018) 941–947.
[145] H.C. Chuang, G.Y. Hong, J. Sanchez, Fabrication of high aspect ratio copper nanowires using supercritical CO2 fluids electroplating technique in AAO template, Materials Science in Semiconductor Processing 45 (2016) 17–26.
[146] H.C. Chuang, H.M. Yang, G.L. Wu, J. Sanchez, J.H. Shyu, The effects of ultrasonic agitation on supercritical CO2 copper electroplating, Ultrasonics Sonochemistry 40 (2018) 147–156.
[147] H.C. Chuang, J. Sanchez, Fabrication of Cu coatings by ultrasound-assisted supercritical argon electroplating, Materials Letters 243 (2019) 54–57.
[148] H.C. Chuang, J. Sanchez, Parametric Characterization of Copper Metal Coatings Produced by Supercritical Argon Electroplating, Jom 72 (2020) 711–720.
[149] X. Xing, N. Li, Y. Sun, G. Wang, J. Cheng, Z. Hao, Selective catalytic oxidation of n-butylamine over Cu-zeolite catalysts, Catalysis Today 339 (2020) 192–199.
[150] M.H. Mahyuddin, Y. Shiota, K. Yoshizawa, Methane selective oxidation to methanol by metal-exchanged zeolites: a review of active sites and their reactivity, Catal. Sci. Technol. 9 (2019) 1744–1768.
[151] H.I. Hamoud, V. Valtchev, M. Daturi, Selective catalytic reduction of NOx over Cu- and Fe-exchanged zeolites and their mechanical mixture, Applied Catalysis B: Environmental 250 (2019) 419–428.
[152] B. Ipek, R.A. Pollock, C.M. Brown, D. Uner, R.F. Lobo, H2 Adsorption on Cu(I)–SSZ-13, The Journal of Physical Chemistry C, 122 (2018) 540–548.
[153] T.D. Pham, Q. Liu, R.F. Lobo, Carbon dioxide and nitrogen adsorption on cation-exchanged SSZ-13 zeolites, Langmuir 29 (2013) 832–839.
[154] P. Chen, V. Rizzotto, A. Khetan, K. Xie, R. Moos, H. Pitsch, D. Ye, U. Simon, Mechanistic Understanding of Cu-CHA Catalyst as Sensor for Direct NH3-SCR Monitoring: The Role of Cu Mobility, ACS Appl Mater Interfaces 11 (2019) 8097–8105.
[155] V. Rizzotto, U. Simon, Effects of Extra-Framework Metal Centers on Zeolite-Based NH3-Sensors for Exhaust Gas Abatement, in: ECS Meeting Abstracts, MA2020-01, 2020, 2132-2132.
[156] M.V. Palmer, S.S.T. Ting, Applications for supercritical fluid technology in food processing, Food Chemistry 52 (1995) 345–352.
[157] G. Brunner, Supercritical fluids: technology and application to food processing, Journal of Food Engineering 67 (2005) 21–33.
[158] G. Brunner, Applications of supercritical fluids, Annu. Rev. Chem. Biomol. Eng. 1 (2010) 321–342.
[159] S.B. Iversen, T. Larsen, O. Henriksen, K. Felsvang, The world's first commercial supercritical wood treatment plant, in: Proceedings of the 6th International symposium on supercritical fluids, Versailles, 2003, pp. 445–450.
[160] E. Weidner, Impregnation via supercritical CO2–What we know and what we need to know, The Journal of Supercritical Fluids 134 (2018) 220–227.
[161] O. Pascu, B. Cacciuttolo, S. Marre, M. Pucheault, C. Aymonier, ScCO2 assisted preparation of supported metal NPs. Application to catalyst design, The Journal of Supercritical Fluids 105 (2015) 84–91.
[162] S. Lang, M. Türk, B. Kraushaar-Czarnetzki, Novel PtCuO/CeO2/α-Al2O3 sponge catalysts for the preferential oxidation of CO (PROX) prepared by means of supercritical fluid reactive deposition (SFRD), Journal of Catalysis 286 (2012) 78–87.
[163] E. Ogel, M. Casapu, D.E. Doronkin, R. Popescu, H. Störmer, C. Mechler, G. Marzun, S. Barcikowski, M. Türk, J.D. Grunwaldt, Impact of Preparation Method and Hydrothermal Aging on Particle Size Distribution of Pt/γ-Al2O3 and Its Performance in CO and NO Oxidation, The Journal of Physical Chemistry C 123 (2019) 5433–5446.
[164] F. Ulusal, B. Darendeli, E. Erünal, A. Egitmen, B. Guzel, Supercritical carbondioxide deposition of γ-Alumina supported Pd nanocatalysts with new precursors and using on Suzuki-Miyaura coupling reactions, The Journal of Supercritical Fluids 127 (2017) 111–120.

[165] B. Tezcan, F. Ulusal, A. Egitmen, B. Guzel, Preparation of metallic Pd nanoparticles using supercritical CO2 deposition: An efficient catalyst for Suzuki cross-coupling reaction, Journal of Nanoparticle Research 20 (2018).
[166] F. Ulusal, E. Erünal, B. Güzel, Green preparation of Pd nanoparticles on SBA-15 via supercritical fluid deposition and application on Suzuki–Miyaura cross-coupling reaction, Journal of Nanoparticle Research 20 (2018).
[167] X.R. Ye, Y.H. Lin, C.M. Wai, Decorating catalytic palladium nanoparticles on carbon nanotubes in supercritical carbon dioxide, Chemical Communications (2003) 642–643.
[168] X.R. Ye, Y.H. Lin, C.M. Wang, M.H. Engelhard, Y. Wang, C.M. Wai, Supercritical fluid synthesis and characterization of catalytic metal nanoparticles on carbon nanotubes, J. Mater. Chem. 14 (2004) 908–913.
[169] Y.H. Lin, X.L. Cui, X.R. Ye, Electrocatalytic reactivity for oxygen reduction of palladium-modified carbon nanotubes synthesized in supercritical fluid, Electrochemistry Communications 7 (2005) 267–274.
[170] Y.H. Lin, X.L. Cui, C. Yen, C.M. Wai, Platinum/carbon nanotube nanocomposite synthesized in supercritical fluid as electrocatalysts for low-temperature fuel cells, Journal of Physical Chemistry B 109 (2005) 14410–14415.
[171] G. Girishkumar, K. Vinodgopal, P.V. Kamat, Carbon nanostructures in portable fuel cells: Single-walled carbon nanotube electrodes for methanol oxidation and oxygen reduction, Journal of Physical Chemistry B 108 (2004) 19960–19966.
[172] J. Zhao, L.Q. Zhang, T. Chen, H. Yu, L. Zhang, H. Xue, H.Q. Hu, Supercritical Carbon-Dioxide-Assisted Deposition of Pt Nanoparticles on Graphene Sheets and Their Application as an Electrocatalyst for Direct Methanol Fuel Cells, Journal of Physical Chemistry C 116 (2012) 21374–21381.
[173] J. Zhao, Z.S. Liu, H.Q. Li, W.B. Hu, C.Z. Zhao, P. Zhao, D.L. Shi, Development of a Highly Active Electrocatalyst via Ultrafine Pd Nanoparticles Dispersed on Pristine Graphene, Langmuir 31 (2015) 2576–2583.
[174] A. Bayrakceken, A. Smirnova, U. Kitkamthorn, M. Aindow, L. Turker, I. Eroglu, C. Erkey, Vulcan-Supported Pt Electrocatalysts for PEMFCs Prepared using Supercritical Carbon Dioxide Deposition, Chemical Engineering Communications 196 (2009) 194–203.
[175] S.E. Bozbag, T. Gumusoglu, S. Yilmazturk, C.J. Ayala, M. Aindow, H. Deligoz, C. Erkey, Electrochemical performance of fuel cell catalysts prepared by supercritical deposition: Effect of different precursor conversion routes, Journal of Supercritical Fluids 97 (2015) 154–164.
[176] Y. Lin, X.C.H. Yen, C.M. Wai, PtRu/Carbon nanotube nanocomposite synthesized in supercritical fluid: a novel electrocatalyst for direct methanol fuel cells, Langmuir 21 (2005) 11474.
[177] M. Watanabe, Y.M. Zhu, H. Igarashi, H. Uchida, Mechanism of CO tolerance at Pt-alloy anode catalysts for polymer electrolyte fuel cells, Electrochemistry Communications 68 (2000) 244.
[178] Y.Z. Zhou, C.H. Yen, Y.H. Hu, C.M. Wang, X.N. Cheng, C.M. Wai, J. Yang, Y. H. Lin, Making ultrafine and highly-dispersive multimetallic nanoparticles in three-dimensional graphene with supercritical fluid as excellent electrocatalyst for oxygen reduction reaction, J. Mater. Chem. A 4 (2016) 18628–18638.
[179] J.M. Bassat, D. Mesguich, C. Ferchaud, Y. Zhang-Steenwinkel, F. van Berkel, C. Aymonier, J.J. Watkins, J.C. Grenier, Doped/Undoped Ceria Buffer Layers for Improved LT-SOFC Performances with Pr2NiO4+delta Cathode, in: S.C. Singhal, K. Eguchi (Eds.), Solid Oxide Fuel Cells, 2011, pp. 1945–1954, 12.
[180] D. Mesguich, C. Aymonier, J.M. Bassat, F. Mauvy, E. You, J.J. Watkins, Low-Temperature Deposition of Undoped Ceria Thin Films in scCO(2) As Improved Interlayers for IT-SOFC, Chemistry of Materials 23 (2011) 5323–5330.
[181] Q.Le Trequesser, D. Mesguich, E. You, C. Aymonier, J.J. Watkins, Supercritical fluid deposition of compositionally uniform yttria stabilized zirconia films, Journal of Supercritical Fluids 66 (2012) 328–332.
[182] T.R. Karl, K.E. Trenberth, Modern global climate change, Science 302 (2003) 1719–1723.
[183] R.a.D.A. Ussiri, Introduction to Global Carbon Cycling: An Overview of the Global Carbon Cycle, in: Carbon Sequestration for Climate Change Mitigation and Adaptation, Springer, Cham, Switzerland, 2017.
[184] C. Genovese, C. Ampelli, S. Perathoner, G. Centi, Electrocatalytic conversion of CO2 on carbon nanotube-based electrodes for producing solar fuels, J. Catal. 308 (2013) 237–249.
[185] C. Ampelli, C. Genovese, M. Errahali, G. Gatti, L. Marchese, S. Perathoner, G. Centi, CO2 capture and reduction to liquid fuels in a novel electrochemical setup by using metal-doped conjugated microporous polymers, J. Appl. Electrochem. 45 (2015) 701–713.
[186] A. Del Castillo, M. Alvarez-Guerra, A. Irabien, Continuous Electroreduction of CO2 to Formate Using Sn Gas Diffusion Electrodes, Aiche J. 60 (2014) 3557–3564.
[187] Q.N. Wang, H. Dong, H.B. Yu, Development of rolling tin gas diffusion electrode for carbon dioxide electrochemical reduction to produce formate in aqueous electrolyte, J. Power Sources 271 (2014) 278–284.
[188] H.R. Jhong, F.R. Brushett, P.J.A. Kenis, The Effects of Catalyst Layer Deposition Methodology on Electrode Performance, Adv. Energy Mater. 3 (2013) 589–599.
[189] J. Medina-Ramos, R.C. Pupillo, T.P. Keane, J.L. DiMeglio, J. Rosenthal, Efficient Conversion of CO2 to CO Using Tin and Other Inexpensive and Easily Prepared Post-Transition Metal Catalysts, J. Am. Chem. Soc. 137 (2015) 5021–5027.
[190] Z. Bitar, A. Fecant, E. Trela-Baudot, S. Chardon-Noblat, D. Pasquier, Electrocatalytic reduction of carbon dioxide on indium coated gas diffusion electrodes-Comparison with indium foil, Appl. Catal. B-Environ. 189 (2016) 172–180.
[191] J.L. Yu, H.Y. Liu, S.Q. Song, Y. Wang, P. Tsiakaras, Electrochemical reduction of carbon dioxide at nanostructured SnO2/carbon aerogels: The effect of tin oxide content on the catalytic activity and formate selectivity, Appl. Catal. A-Gen. 545 (2017) 159–166.
[192] M.T. Mehran, S.B. Yu, D.Y. Lee, J.E. Hong, S.B. Lee, S.J. Park, R.H. Song, T. H. Lim, Production of syngas from H2O/CO2 by high-pressure coelectrolysis in tubular solid oxide cells, Appl. Energy 212 (2018) 759–770.
[193] C. Jimenez, J. Garcia, R. Camarillo, F. Martinez, J. Rincon, Electrochemical CO2 Reduction to Fuels Using Pt/CNT Catalysts Synthesized in Supercritical Medium, Energy & Fuels 31 (2017) 3038–3046.
[194] J. Garcia, C. Jimenez, F. Martinez, R. Camarillo, J. Rincon, Electrochemical reduction of CO2 using Pb catalysts synthesized in supercritical medium, Journal of Catalysis 367 (2018) 72–80.
[195] C. Jiménez, J. García, F. Martínez, R. Camarillo, J. Rincón, Deposition of Cu on CNT to synthesize electrocatalysts for the electrochemical reduction of CO2: Advantages of supercritical fluid deposition technique, The Journal of Supercritical Fluids 166 (2020), 104999.
[196] C. Jiménez, J. García, F. Martínez, R. Camarillo, J. Rincón, Cu nanoparticles deposited on CNT by supercritical fluid deposition for electrochemical reduction of CO2 in a gas phase GDE cell, Electrochimica Acta 337 (2020), 135663.
[197] J.-W. Wu, C.-H. Wang, Y.-C. Wang, J.-K. Chang, Ionic-liquid-enhanced glucose sensing ability of non-enzymatic Au/graphene electrodes fabricated using supercritical CO2 fluid, Biosensors and Bioelectronics 46 (2013) 30–36.
[198] C.-H. Wang, S.-W. Lee, C.-J. Tseng, J.-W. Wu, I.M. Hung, C.-M. Tseng, J.-K. Chang, Nanocrystalline Pd/carbon nanotube composites synthesized using supercritical fluid for superior glucose sensing performance, Journal of Alloys and Compounds 615 (2014) S496–S500.
[199] C.-H. Wang, C.-H. Yang, J.-K. Chang, High-selectivity electrochemical non-enzymatic sensors based on graphene/Pd nanocomposites functionalized with designated ionic liquids, Biosensors and Bioelectronics 89 (2017) 483–488.